Momentum flux characteristics of vertical propagating Gravity Waves

Prosper K. Nyassor[1], Cristiano M. Wrasse[1], Igo Paulino[2], Erdal Yiğit[3], Cosme A. O. B. Figueiredo[2], Ricardo A. Buriti[2], Fábio Egito[2], Hisao Takahashi[1], Gabriel A. Giongo[1], Delano Gobbi[1], and Oluwasegun M. Adebayo[1]

[1]Space Weather Division, National Institute of Space Research (INPE), São José dos Campos, Brazil
[2]Academic Unit of Physics, Federal University of Campina Grande (UFCG), Campina Grande, Brazil
[3]Department of Physics and Astronomy, George Mason University, Fairfax, VA, USA

Correspondence: Prosper K. Nyassor (prosper.nyassor@inpe.br)

Abstract. Simultaneous observations of airglow intensity, rotational temperature, and wind data at São João do Cariri (36.31°W; 07.40°S) by Co-located photometer, all-sky imager, and meteor radar were used to study the characteristics of vertical propagating gravity waves (GWs). Using the photometer data, the phase progression of GWs with the same propagation period in the OI 5577, O_2, NaD - line, and OH emission layers were then used to determine the vertical propagation of the waves. The vertical phase speed and wavelength are estimated using the wave period and phase difference at different altitude. Due to little or no phase difference across the emission layers, the background propagation conditions are examined. It was observed that the presence of a duct most likely contributed to near vertical propagation of the observed GWs. Next, the dynamics of the GWs in such condition was investigated using the momentum and energy. From the O_2 and OH rotational temperatures, the momentum flux and potential energy of the propagating GWs were determined. Further analysis revealed that the momentum flux and potential energy of the propagating GWs is higher in the O_2 emission layer than in the OH emission layer. Thus, demonstrating the transfer of momentum and energy.

1 Introduction

The vertical propagation of atmospheric gravity waves (GWs) is known to be the main transport mechanism of momentum and energy into the upper atmosphere (Fritts and Alexander, 2003; Yiğit et al., 2016). Owing to the decrease of density with altitude, amplitudes of GWs increase exponentially if dissipation/wave breaking does not occur. GWs are excited by flows surging up mountains (e.g., Gossard and Hooke, 1975; Lindzen, 1984), fronts and jet streams (e.g., Lindzen, 1984; Fritts and Alexander, 2003; Wrasse et al., 2024), convective layers (e.g., Townsend, 1966), deep convection thunderstorms (e.g., Taylor and Hapgood, 1988; Fritts and Alexander, 2003; Sentman et al., 2003; Yue et al., 2009; Vadas et al., 2009; Nyassor et al., 2021, 2022a, b), volcanoes (e.g., Yue et al., 2022; Figueiredo et al., 2023), typhoons (e.g., Li et al., 2022; Chou et al., 2017),

by earthquakes (e.g., Heale et al., 2020), solar eclipses (e.g., Paulino et al., 2020, and references therein) and other process that cause unbalance between the gradient of pressure and the buoyancy. The waves then propagate both horizontally and vertically (Becker and Schmitz, 2003).

Vertical propagation characteristics of gravity waves are controlled by background temperature and wind relative to the horizontal phase speed of waves as well as by wave dissipation due to nonlinear diffusion, viscosity, and ion drag (Yiğit et al., 2008, 2021). Depending on wave interaction with the background field, the waves can be classified as a ducted, propagating, or evanescent modes (Gossard and Hooke, 1975). Some of these waves suffer critical level filtering when propagating waves encounter an equal vector of background wind, where the wave can be absorbed by the background Heale and Snively (2015). Otherwise, it can be reflected if the gravity wave encounters a strong wind in the opposite direction. According to Fritts and Alexander (2003), reflected waves from the upper and (or) lower altitude regions can be (partially) ducted. GWs are filtered in the middle and lower thermosphere (MLT) region during breaking. Vertical propagating waves interact with the mean flow through the transfer of momentum and energy dissipation when breaking (Lindzen, 1981; Holton, 1982), particularly in the mesosphere. Thus, these waves significantly contribute to atmospheric circulation and dynamical fields of temperature and wind (Le Du et al., 2022; Yiğit and Medvedev, 2009).

Horizontal and vertical propagation of GWs are greatly influenced by the background wind and temperature fields (Nappo, 2013). The background fields can either hinder or favor the vertical propagation of the wave. Doppler or thermal ducts favor longer horizontal propagation of GWs (Bageston et al., 2011; Snively et al., 2007; Snively and Pasko, 2008) whereby hindering the vertical propagation. Vertical propagating GWs can either be upward (vertical wavenumber lower than zero, $m < 0$) or downwards ($m > 0$), where energy and momentum are transported in either direction. A typical example is the vertical propagation of secondary GWs which resulted from primary GWs breaking and/or dissipation in the MLT (Vadas et al., 2003; Medvedev et al., 2023). During the breaking/dissipation of primary GW, energy and momentum are released, which are further transported upward and downward as they propagate (Vadas et al., 2003).

Several observational techniques (e.g., Suzuki et al., 2013) have been employed to study the vertical propagation of GWs. Observation techniques such as Lidar (Suzuki et al., 2013), radiosonde (Schöch et al., 2004; Sato and Yoshiki, 2008; Yamashita et al., 2009) among others, have been used. In the mesosphere, Nyassor et al. (2018) used an airglow photometer to study the vertical propagation of GWs. According to Nyassor et al. (2018, and references therein), simultaneous observation of multiple airglow emissions is one of the techniques used to investigate the vertical propagation of gravity waves in the mesosphere. This technique is possible if and only if the vertical wavelengths of the wave are larger than the thickness of the airglow emission layer (Nyassor et al., 2018, and references therein). Such observational data can be used to determine the propagation characteristics and amplitude growth of gravity waves (Taori et al., 2005).

In this research, the characteristics of the momentum flux and energy of vertical (upward and downward) propagation of GWs are examined. This work is conducted using principally data from multiple airglow emissions observation by photometer similar to the work of Nyassor et al. (2018). Observations of GWs propagating through the emissions: atomic oxygen green line (OI 557.7 nm), molecular oxygen (O_2 - 864.5 nm), sodium D-line (NaD-589.0 nm), and hydroxyl (OH) (6 - 2) band. GWs with the same period propagating through all the four (4) emission layers were selected for this study. Using complementary

observations from co-located all-sky imager and meteor radar, the characteristics of GW energy and momentum flux with altitude are explored. As, the characteristics of GW energy and momentum flux of upward propagating waves are well known and explored, other aspects of the dynamics of momentum and energy transported in different propagating conditions are intended to be studied in this work.

2 Observation and data analysis

2.1 Airglow

Airglow is a natural upper atmospheric phenomenon in which light are emitted due to de-excitation of atomic and ionic constituents from higher to lower energy levels. Physical causes of airglow includes chemical reaction of neutral constituents of the upper atmosphere and reactions involving ionized constituents. Though other mechanisms do exist, these two are omnipresent and contribute to the light of the night sky (Roach, 2013). Airglow is among the atmospheric tracers used in the study of atmospheric waves. In this work, the dynamics of GWs in the mesosphere are studied using airglow modulated intensities by GWs in the hydroxyl (OH (6 - 2), hereafter OH), sodium D-line (NaD-Line, hereafter NaD), molecular oxygen (O_2 (0 - 1), hereafter O_2) and atomic oxygen (OI 557.7 nm, hereafter OI 5577) emission layers.

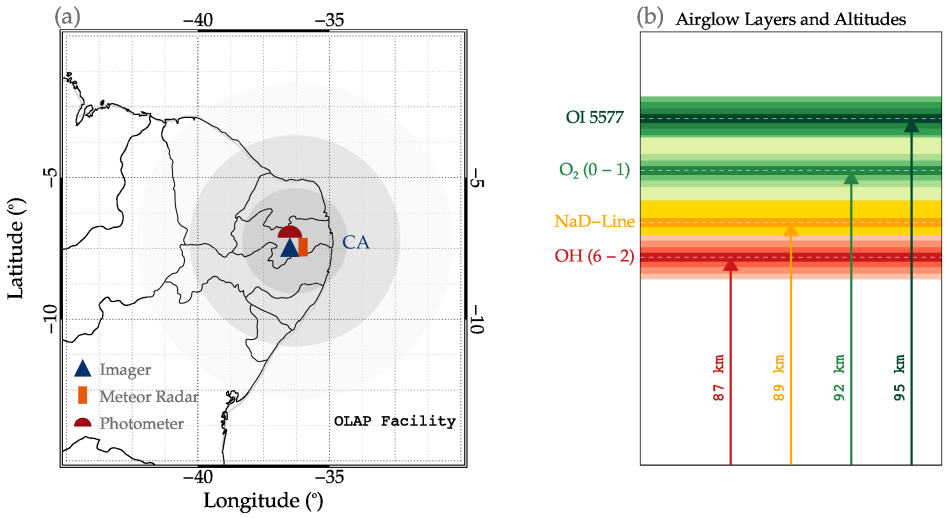

Figure 1. (a) Geographical location of the observatory and co located instruments, as well as the imager field of view of each airlgow layer. The dark blue triangle, orange filled vertical rectangle and red filled semi-circle represent position of the all-sky imager (imager), meteor radar and photometer, respectively. The deep gray shaded region indicates a radius of 256 km. The medium gray circular shaded region indicate the field of view of the imager (with a radius of 512 km) whereas light shaded region shows a radius of 768 km. (b) Airglow emission layers and their respective altitudes. The red, gold, light green and deep green respectively represent the hydroxyl (OH), sodium D-line (NaD), molecular oxygen atmospheric band (O_{0-1}) and the green line atomic oxygen (OI 5577) emission layers. Each respective dark colors with white horizontal dashed lines indicate the peak altitude of each emission layer as indicated by the corresponding labeled vertical arrows.

The peak altitudes of OH, NaD, O_2, and OI 5577 are ∼87 km ($\Delta z = 8$ km), ∼90 ($\Delta z = 8$ km), ∼92 ($\Delta z = 8$ km) and ∼95 km ($\Delta z = 8$ km), respectively. Figure 1(a) shows the location of the Paraíba Atmospheric Luminescence Observatory, in Portugese, Observatório de Luminescência atmosférica da Paraíba (OLAP) where the photometer, all-sky imager (hereafter, imager) and meteor radar used in this research are hosted. In Figure 1a. The dark blue triangle, orange filled vertical rectangle and red filled semi-circle represent position of the imager, meteor radar and photometer, respectively. The deep gray shaded region indicates a radius of 256 km. The medium gray circular shaded region indicate the field of view of the imager (with a radius of 512 km), whereas light shaded region shows a radius of 768 km.

The airglow emissions with the peak emission depicted in dark horizontal lines and altitude range (Δz) of each emission layer in their respective faint colors is presented in Figure 1(b). The red, gold, light green and deep green represent the hydroxyl (OH), sodium D-line (NaD), molecular oxygen atmospheric band (O_2) and the green line atomic oxygen (OI 5577) emission layers, respectively. The respective dark colors with white horizontal dashed lines indicate the peak altitude of each emission layer as indicated by the corresponding labeled vertical arrows. Using instruments such as, airglow photometers and imagers with distinct bandpass filters, each emission layer can be observed. For this work, variations in the airglow intensity of these four emission layers shown in Figure 1(b) are used.

2.1.1 Airglow Photometer

The airglow photometer used in the observation of the mesospheric airglow emissions is located at São João do Cariri (36.31°W; 07.40°S). The photometer is a multi-channel tilting filter photometer (Multi-3) with five interference filters. The background continuum intensity (R nm^{-1}) and the line intensity (R) were measured to obtain the zenith sky spectrum by tilting the filters relative to their optical axes in which a scan of a wavelength of about 8 nm was made. The mesospheric component of the OI 5577 was estimated by removing the effect of the simultaneous observation of OI 630.0 nm (hereafter, OI 6300) intensity in the ionospheric F-region component computed as 20% (Silverman, 1970). The temporal resolution of the observation is 2 minutes, thus GWs with periods greater than 2 minutes can be observed. The photometer characteristics, that is, calibration scheme and error, spectral resolution, and sensitivity, can be seen in Nyassor et al. (2018, and references therein).

An observation scheme of 13 nights per month centered around the time of the new moon was made with more than 6 h of continuous observation time per night. The observational data used for this study extend from January 2000 to December 2007, which resulted in a total of clear sky observation nights of 1051. Details on the Multi-3 filter photometer can be found in Wrasse et al. (2004) and references therein. The database of OI 5577, O_2, NaD - Line, and OH was analyzed to find GWs propagating with same period in each emission altitude. Among the total nights of clear sky night observation, 389 nights present similar periods in at least two emission layers, of which 24 nights present similar periods in three emission layers. For this study, 2 GW events with the same period in all the 4 emission layers are selected. The photometer is used for airglow intensity observation and for the rotational temperature of the O_2 and OH emission layers (Buriti et al., 2001).

2.1.2 Atmospheric Bands Rotational Temperatures derived from OH (6 - 2) Meinel and O_2 (0 - 1)

The complex rotational band spectrum of the OH and O_2 emission permits the determination of mesospheric temperatures by measuring the intensity distribution between various spectral lines in the bands (Innis et al., 2001). The collision frequency of OH with the neutral atmosphere near 90 km of altitude has been shown to be of the order of $10^4\ s^{-1}$ with a lifetime of the excited OH being around 3 - 10 ms (Mies, 1974). This indicates that the excited OH molecules in the rotational energy levels are in thermal equilibrium with the atmospheric ambient gas (Sivjee and Hamwey, 1987; Takahashi et al., 1998) and thus, a good proxy for atmospheric temperature studies. The OH rotational line spectra is an open structure with separation of 1 - 2 nm between the lines, which makes it easy to measure individual lines with a low resolution (of $\sim$1 nm) spectrometer. Further, the line intensities of most of the bands are only a function of the rotational temperature. Thus, using two lines from a single band, the rotational temperature can be estimated using the following equation Mies (1974):

$$T_{n,m} = \frac{E_{\nu'}(J'_m) - E_{\nu'}(J'_n)}{k_B In\left[\frac{I_n}{I_m}\frac{A(J'_m,\nu'\rightarrow J''_{m+1},\nu'')}{A(J'_n,\nu'\rightarrow J''_{n+1},\nu'')}\frac{2J'_m+1}{2J'_n+1}\right]}, \quad (1)$$

where, $T_{n,m}$ is the rotational temperature estimated from two intensity lines, I_n and I_m, from rotational levels J'_n, J'_m in the upper vibrational level ν', to J''_{n+1}, J''_{m+1} in the lower vibrational level ν''. $E_\nu(J)$ is the energy of the level (J,ν). $A(J'_n,\nu' \rightarrow J''_{n+1},\nu'')$ is the Einstein coefficient, for the transition from J'_n,ν' to J''_n,ν''. k_b is the Boltzmann Constant.

Molecular oxygen also satisfies the local thermal equilibrium (LTE) similar to OH bands, which makes it possible for the estimation of the rotational temperature. O_2 is known to have a lifetime of more that $\sim$10 sec, making it capable of attaining the LTE. The rotational temperature can also be determined using a similar procedure of OH rotational temperature.

2.2 All-Sky Imager

An all-sky imager was used to determine the horizontal component of the GWs observed by the photometer. Images of OH, O_2, OI 5577, and OI 6300 airglow emission layers were taken by this equipment. With regard to this work, only the OH and O_2 bands airglow images corresponding to the selected coincident photometer observation were used. The airglow all-sky imager is an optical instrument made of a fast fish-eye (f/4) lens, a telecentric lens system, a filter wheel, and a charged coupled device (CCD) camera. The CCD camera has an area of 6.04 cm^2 with a 1024×1024 back-illuminated pixel array of 14 bits per pixel. In order to enhance the signal-to-noise ratio, the images were binned on chip down to a resolution of 512×512. The high quantum efficiency, low dark noise (0.5 electrons $pixel^{-1}s^{-1}$), low readout noise (15 electron rms), and high linearity (0.05 %) of this device enable it to measure airglow emissions (Nyassor et al., 2018; Medeiros et al., 2003).

2.3 Meteor Radar

Background winds from a SKiYMET all-sky interferometric meteor radar with a two-element receiving and three-element transmitting antenna were used to observe mesospheric winds. The meteor radar operates at the same location of the photometer and make observations between 82 and 98 km. This radar operates at a frequency of 35.24 MHz with a maximum transmitter power of 12 kW. The respective temporal and vertical resolutions of this radar are typically 60 min and 1 km. The observation characteristics of the radar have been published elsewhere in Nyassor et al. (2018, and references therein) and Lima et al. (2004).

3 Methodology and Data Analysis

3.1 Photometer Time Series

The methods to obtain the final result of the photometer data include (i) preprocessing, (ii) processing, (iii) parameterization, and (iv) discussion. A graphical demonstration of these procedures is shown in the flowchart in Figure 2.

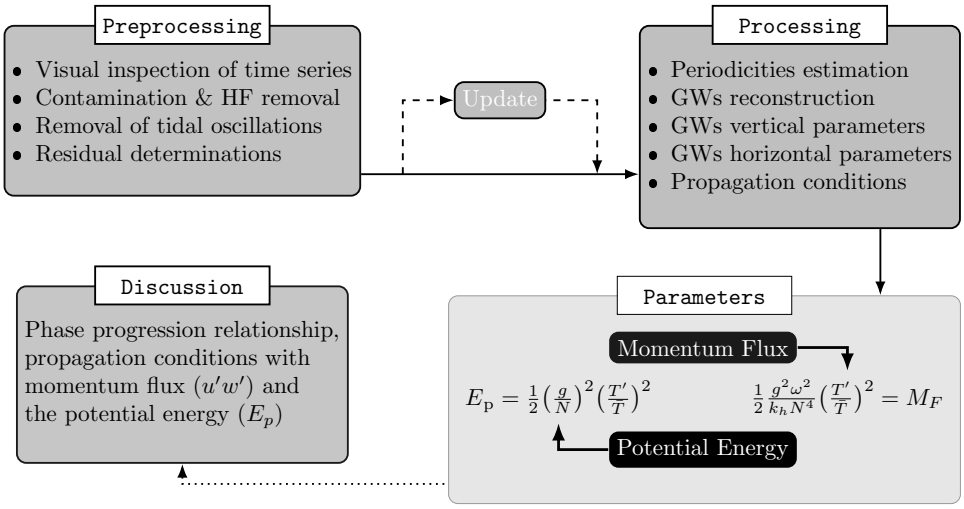

Figure 2. Flowchart showing airglow photometer data processing procedures and GW characterization. The procedure includes preprocessing, processing, parameterization, and discussion.

3.2 Preprocessing

This preprocessing stage involves four steps, as outlined in Figure 2. Firstly, the time series is made up of the variations of wave oscillations and those due to contaminants. Hence, there is a need for visual inspection to detect any of these contaminants that appear as spikes in the time series. The contaminants can be due to artificial light sources, clouds, or astronomical lights passing across the field of view of the photometer. In Figure 3, the hours are in universal time (UT) and span from 18:00 UT on 04 December 2004 to 28 (04:00 UT) on 05 December 2004. In Figure 3(a), a typical spike due to contaminant is highlighted in red. Also, gaps are usually found in the data due to instrumental problems (however, no gaps exist for this data). A criterion is set such that if the gaps or spikes in the data set are interrupted frequently in order of minutes, the data set will be disregarded. Spikes are removed from the dataset. If the clean data (data without spikes) has a continuous observation for less than 3 hours, the event of that night is disregarded. Due to the spike (the blue highlighted region) in the time series in Figure 3a, the data is limited to 23:00 UT on 04/05/2004 to 03:00 UT on 05/05/2004.

Clean time series with continuous observations of more than 3 hours are considered for further analysis. Next, high frequency oscillations are removed by applying a three-point running mean. Figure 3b shows the clean and smooth (three-point averaged) data. Finally, to obtain a dataset with only GW oscillations since GWs are modulated by tides, a harmonics for semidiurnal and terdiurnal tides is constructed using Equation 2 (red solid line in Figure 3(c)).

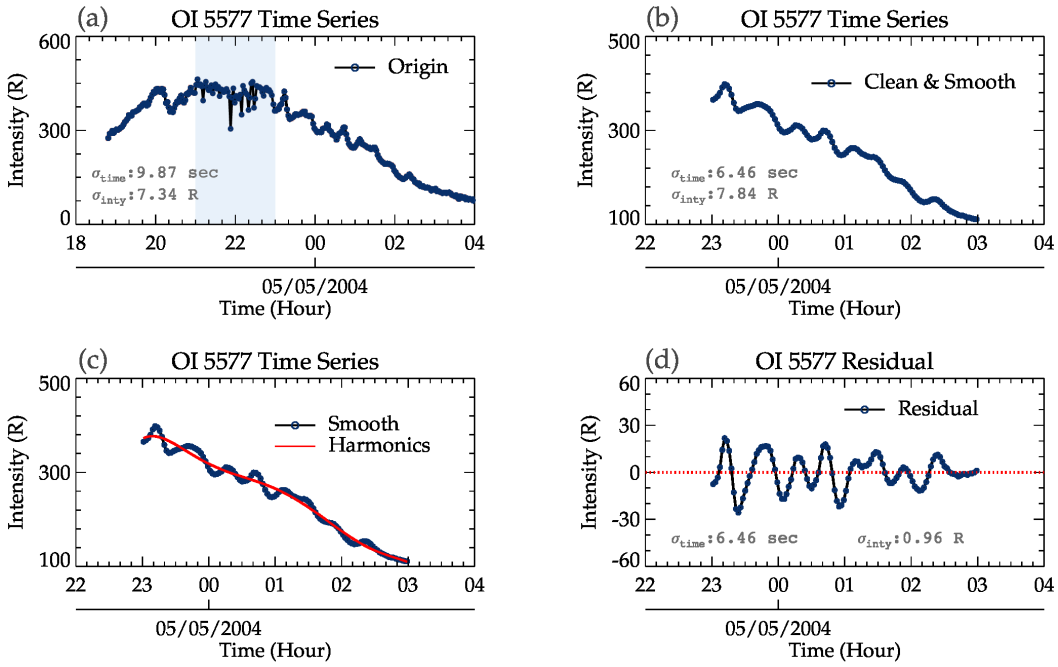

Figure 3. A step-by-step procedure of the preprocessing stage of a photometer data. Panel (a) is the original OI 557.7 nm time series with light blue shaded region indicating the parts of the time series with spikes. In panel (b), the clean and smooth time series is presented. The harmonics of tides, semidiurnal and terdiurnal (red solid line), are constructed and shown in panel (c). The residual (difference between the harmonics and clean-smooth) in (c) is shown in panel (d).

The harmonic is subtracted from the smoothed time series to obtain a time series of the residual (purely GWs). The residual is then used to investigate the vertical propagation of GWs.

$$Y = A + B_i cos\left(\frac{2\pi(x-\phi_i)}{\tau_i}\right) \tag{2}$$

where A and B_i are the unknown amplitude, x is the observation time series, ϕ_i is the phase, and τ_i is the period. i represent the number of periods, which in this case is the periods of semidiurnal ($\tau = 12$ h) and terdiurnal ($\tau = 8$ h).

3.3 Processing

In the processing stage, the first step is to inspect if the four emission layers have been modulated by the same GW. This is done by plotting the intensity variations. In Figure 4a, the temperature (for OH and O_2) and airglow intensity (for OH, Na D-line, O_2 and OI 5577) variations due to the GW modulations between 23:00 UT on 04/12/2004 and 03:00ÙT on 05/12/2004 are presented. The temperature and intensity variations for each emission layer is defined in the respective legends. A similar variation with time was observed in the temperature even though the temperature of the OH is higher than that of O_2. In the

case of airglow intensities, a well-defined similarities due to the presence of GWs was observed. All the variations of the temperature and intensity presented a down-phase progression with time except OH variations.

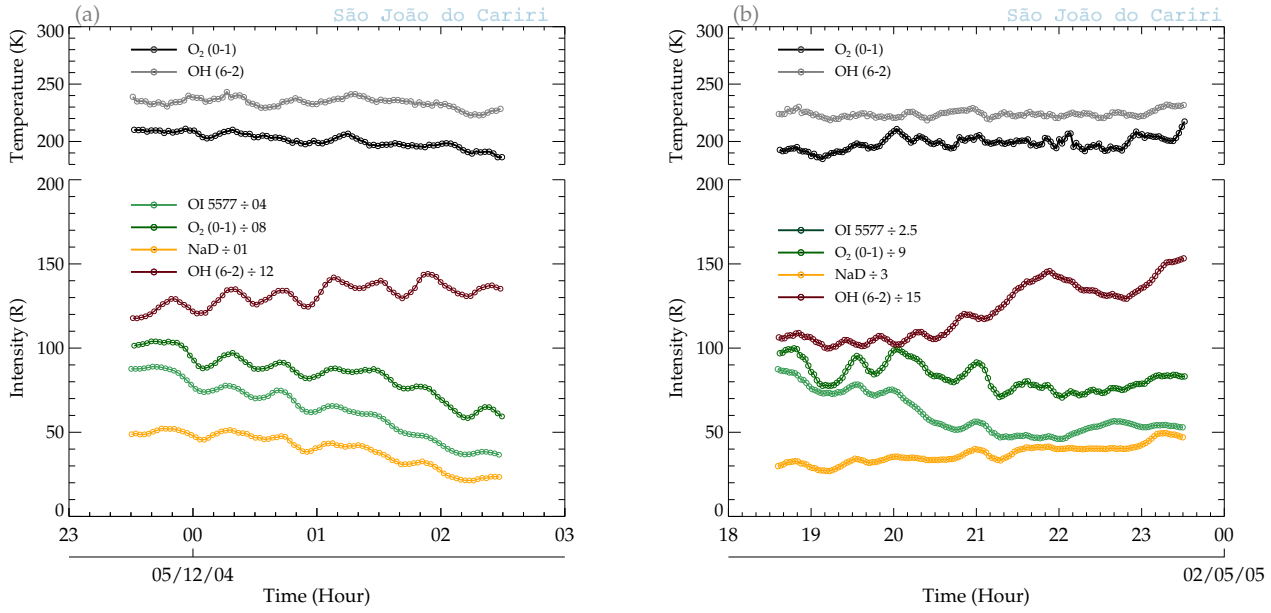

Figure 4. Temperature and airglow intensity variations within 23:00 UT on 04/12/2004 to 03:00 UT on 05/12/2004 and 18:30 to 23:30 UT on 01/05/2005.

The temperature and intensity variations due to GWs modulation for a second case observed between 18:30 and 23:30 UT on 01/05/2005 is presented in Figure 4b. Similar oscillations can be seen in the variations of the temperatures and the intensities. Unlike the case presented in Figure 4a, the O_2 and OH temperature variations present an almost an upward phase progression. A similar characteristics can be found in the variation of the NaD and OH intensity variations. In contrast, the intensity variations of the OI5577 nm and O_2 presents a downward phase progression.

In the processing stage, the residuals were subjected to Lomb-Scargle periodogram and Wavelet analysis to determine the dominant periods in the time series of each emission layer. In Figures 5 and 6, the usable time series, residual and the Lomb-Scargle periodogram for all intensities and rotational temperatures of the emission layers for the GW events for 04 - 05/12/2004 and 01/05/2005 are presented, respectively. In panel (a) of Figures 5 and 6, the intensity and temperature time series (similar to Figure 3c) is shown whereas, the residuals are presented in panel (b). The red solid line in panel (a) indicates the tidal harmonics. The subpanels (iii) and (vi) with gray background represent the respective rotational temperatures of O_2 and OH emission as well as their residual and Lomb-Scargle periodogram. Subpanels (i), (ii), (vi), and (v) represent the usable, residual and Lomb-Scargle periodogram of OI 5577, O_2, NaD, and OH intensities.

In panel (c), the Lomb-Scargle periodogram of each intensity and the respective O_2 and OH rotational temperature are presented. As mentioned earlier, at least two similar/same periods present in each emission layer are selected. The chosen periods are demarcated by vertical dashed lines. It can be seen that almost three similar periods were present, however only

two were used in the follow up analysis. This is because the differences in the emission layers are quite large, especially for the OI 5577 emission intensity and the OH rotational temperature.

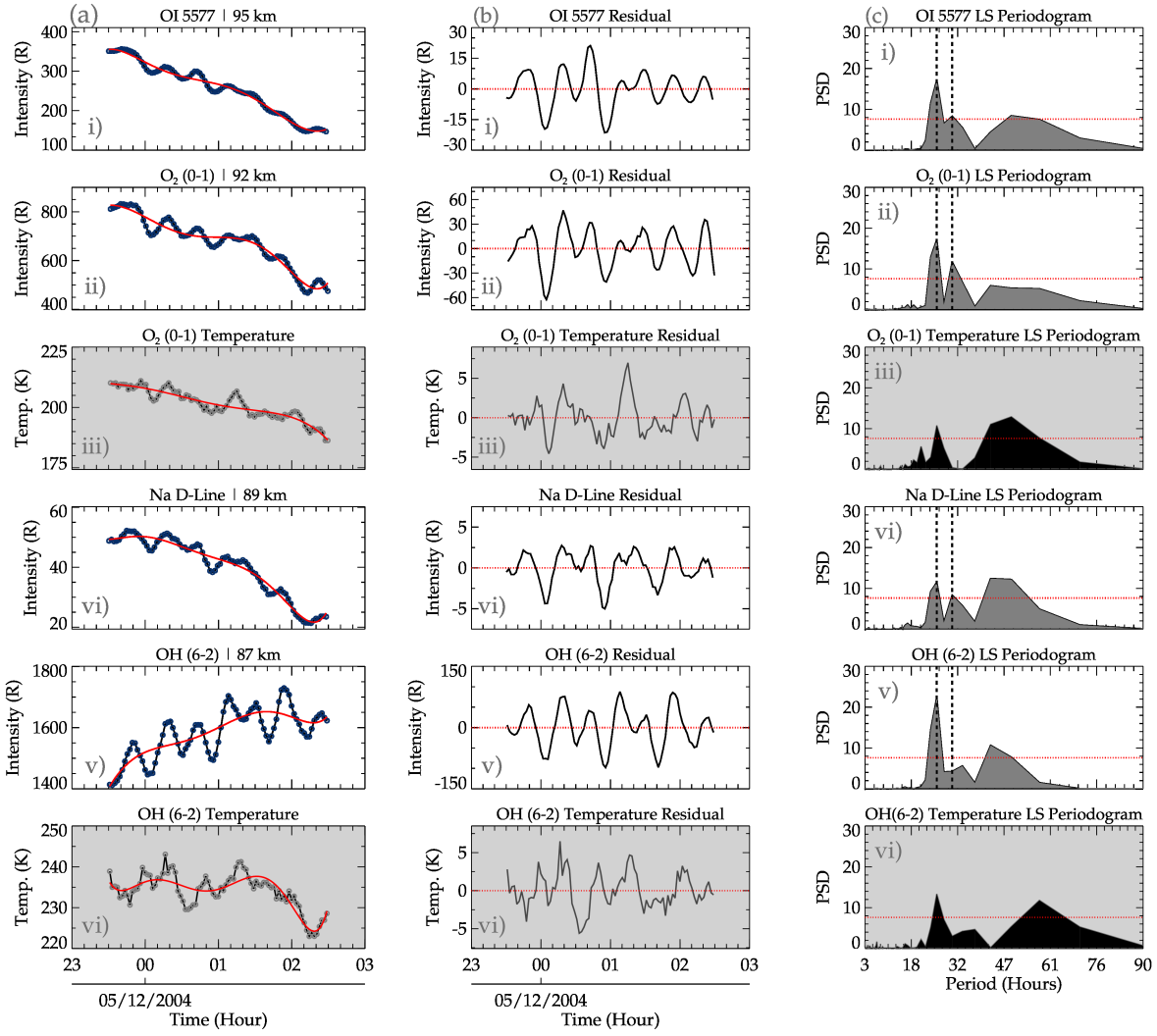

Figure 5. The detailed description of the processing stage of the preprocessed data (obtained form Figure 3). The reconstructed harmonics of the tidal wave oscillations (red solid line) using the dominant periods of 24, 12, and 8 hours and the intensity variations due to GW modulation for each airglow emission layer and those with their rotational temperature are presented in panel (a). The intensity residuals of only GW oscillation are shown in panel (b). In panel (c), the Lomb-Scargle periodogram and Wavelet analysis result of each emission layer intensity and the rotational temperature of O_2 and OH are presented. The red horizontal dotted lines represent 95% significant level.

Similar to Figure 5, Figure 6 presents the processing stage of the GW event of 01/05/2005. For this event, the three (3) dominant periods were detected. For the first period, OI, O_2 and NaD present 0.535477 h (32.13 min), whereas, OH $\sim$ 0.503125 h

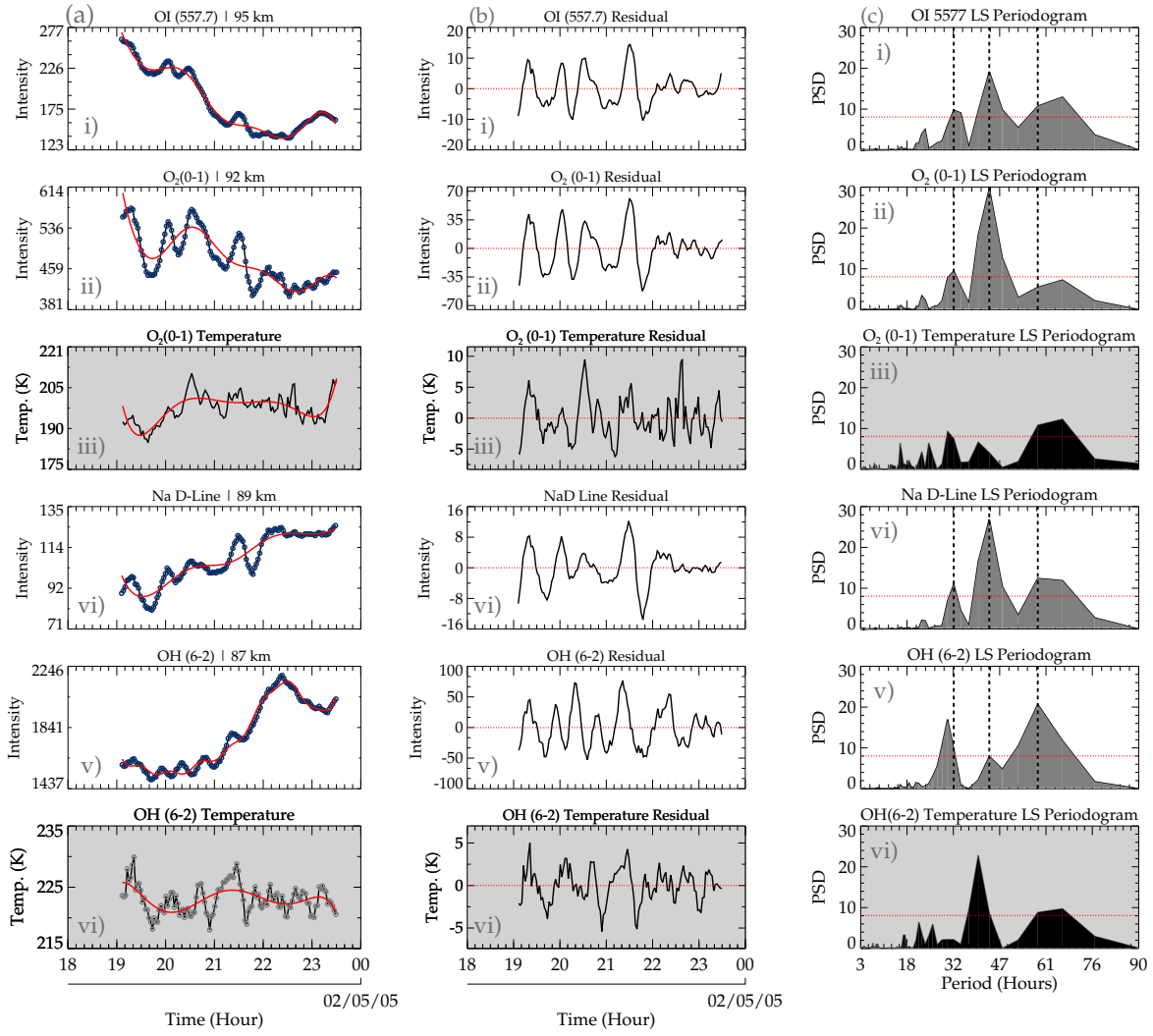

Figure 6. Figure 6 is similar to Figure 5 except for the 01/05/2005 between 18:30 and 23:30 UT.

(30.19 h). The second and third dominant periods $\sim$ 0.720896 h (43.25 min) and $\sim$ 1.10274 h (66.16 min), respectively are present in all the emission layers. The periods are indicated by the vertical black dashed lines.

From the above description, at least two dominant peaks are chosen and used to reconstruct new harmonics and over plotted on the residual. The new harmonics is then normalized and plotted in order of increasing altitude, i.e., 87, 89, 92, and 95 km. Note that the rotational temperature of OH (6 - 2) and O_2 were also subjected to the Lomb-Scargle and Wavelet analysis in order to verify that the temperature was also modulated by the observed GWs. From the reconstructed time series and according to their altitude, the phases (ϕ) of the GWs at each altitude were determined.

The phase (ϕ) is estimated from the Equation 2 and is given in decimal hours. However, the phase needs to be estimated considering the start time of the data being used. This is to give the phase in relation to the start time of the time series. This is done by adding the individual dominant period in the time series until it corresponds to the first hour that corresponds to the start time of the data of each emission layer. For instance, the phase of the 04/12/204 OI GW event is 0.0744475 h for GWs with a period of 0.424451 h ($\sim$25.47 min). The phase in this form in relation to the time of observation, thus the period is added to the phase until 23.419253 h (23:25:00 UT) was attained. This is the time corresponding to the first hour of the time series used. A similar procedure was applied to the intensities of the other emissions layers. In Table 1, the result of the phases of the two waves selected for event #01 and three selected waves for event #02 are presented. The phase shifts were determined from the phases determined from each individual emission layers. The phase shifts are then estimated between each two consecutive layers as well as the first and the fourth layers.

Table 1. Estimated phases (in hours) in each emission layer of the 04-05/12/2004 and 01/05/2005 GW events. The subscripts τ of ϕ indicate the phase of the corresponding periods.

Events	**Phases ϕ**	**OI**	**O_2**	**NaD**	**OH**
Event #01	$\phi_{\tau=25.24}$ (h)	23.419253	23.417403	23.829630	23.419026
	$\phi_{\tau=38.00}$ (h)	23.259999	23.312784	23.293561	23.683039
Event #02	$\phi_{\tau=31.64}$ (h)	18.880139	18.888510	18.856413	18.844777
	$\phi_{\tau=43.25}$ (h)	18.560785	18.573995	18.565454	18.565454
	$\phi_{\tau=58.43}$ (h)	18.570727	18.548215	18.465382	18.379787

The error associated with each emission layer has been performed to evaluate the impact on the result obtained. The error was assessed by estimating the standard error in the original data, the smoothed data and the harmonics. It is important to mention that the estimated standard error of the mean (σ_M) for OI 5577, O_2, NaD and OH intensities (σ_{M_I}), temperature (σ_{M_T}) and time ($\sigma_{M_{time}}$) are presented in Table 2. The standard errors are estimated for original data, clean and usable data, residual and the harmonics.

Table 2. Associated mean standard errors in the time series of the observation hour ($\sigma_{M_{time}}$) in seconds, intensity (σ_{M_I}) in Rayleigh and temperature (σ_{M_T}) in Kelvin for the events of 04/12/2004 and 01/05/2005.

Errors	**Event #01**				**Event #02**			
	OI	**O_2**	**NaD**	**OH**	**OI**	**O_2**	**NaD**	**OH**
Original Data								
$\sigma_{M_{time}}$ (s)	± 09.871	± 09.871	± 09.871	± 09.871	±06.786	±06.786	±06.786	±06.786
σ_{M_I} (R)	±07.339	± 14.745	± 04.076	± 23.243	±03.350	±04.316	±01.110	±18.508
σ_{M_T} (K)		± 01.728		± 03.132		±00.471		±00.186
Usable Data Range								
$\sigma_{M_{time}}$ (s)	± 05.604	± 05.604	± 05.605	± 05.604	±06.786	±06.786	±06.786	±06.786
σ_{M_I} (R)	± 06.958	± 10.911	± 01.052	± 07.998	±03.350	±04.316		±01.110
σ_{M_T} (K)		± 00.670		± 00.413		±00.471		±00.186
Residual								
$\sigma_{M_{time}}$ (s)	± 05.604	± 05.604	± 05.605	± 05.604	±06.786	±06.786	±06.786	±06.786
σ_{M_I} (R)	± 00.964	± 02.537	± 00.203	± 05.024	±00.474	±02.114	±00.410	±02.727
σ_{M_T} (K)		± 00.236		± 00.253		±00.289		±00.172
Harmonics								
σ_{M_H} (R)	± 00.732	± 01.993	± 00.132	± 03.850	±00.411	±01.901	±00.380	±02.256

From Table 2, the estimated errors in the time, intensities and temperature of the original data, clean and usable data, residual and the harmonics are presented. In general, the errors associated with the original data is higher than that of the usable data and the residual. These values are however, less than the measurement errors of the intensities which is of the order of 5% whereas for intensities and 2 - 3 K for O_2 and 4 - 5 K for OH (Wrasse et al., 2004). The error associated with the fit was evaluated by estimating the cross correlation between the time series of the residual of the intensities and temperature and their respective harmonics are indicated in Figure 7 and 8. The cross correlation of the intensities, that is, their residuals and harmonics ranged are 0.76, 0.79, 0.65 and 0.77 for IO, O_2, NaD and OH intensities, respectively. For the temperature residuals and harmonics for O_2 and OH are 0.52 and 0.67, respectively.

Using the differences in phase and altitude between each of the two consecutive emission layers, the average vertical wavelength (λ_z) of the wave is given by Nyassor et al. (2018)

$$\lambda_z = \frac{V_z}{\tau}, \tag{3}$$

where $V_z = \Delta d/\Delta\phi$ is the vertical velocity, with Δd being the difference between the higher and lower emission layers and their respective phases $\Delta\phi$ and τ is the period. A typical result obtained from the procedures in the processing stage is presented in Figure 7 and 8 in Section 4.

3.4 Parameters

In the parameter stage, the potential energy (E_p) and momentum flux ($u'w'$) of the GWs were estimated. The potential energy is estimated using the approach of Narayanan et al. (2024):

$$E_p = \frac{1}{2}\left(\frac{g}{N}\right)^2\left(\frac{T'}{\overline{T}}\right)^2 \tag{4}$$

where g is the gravitational accelerations, N is the Brünt Väisäla frequency, T' is the GWs perturbations, $\overline{T}$ is the background temperature and T' is the temperature variation due GW perturbation. The Brünt Väisäla frequency is defined according to Wrasse et al. (2024) as

$$N = \left(\frac{g}{\theta}\frac{d\theta}{dz}\right)^{1/2}, \tag{5}$$

and

$$\theta = T\big(P/P_0\big)^{R/c_p} \tag{6}$$

where θ is the potential temperature with p and p_o being pressure and reference pressure, respectively. R is the gas constant, and the c_p is the heat capacity at constant pressure. During this wave event, SABER (Sounding of the Atmosphere using Broadband Emission Radiometry) instrument onboard the TIMED (Thermosphere Ionosphere Mesosphere Energetics Dynamics) satellite, made a passage ∼735 km away from the OLAP observation site. The temperature profiles obtained from the SABER sounding are used in the study of the propagation conditions of each selected GW event of this studies. The measured pressure from SABER observation were used in the determination of the potential temperature, where $K/c_p = 0.286$. Using a first order derivative procedure in interactive data language - IDL (Bowman, 2006), the $d\theta/dz$, profile were determined. The potential temperature is the peak altitude of OH and O_2, which are ∼87 and ∼92 km where chosen. However, the IDL procedure requires three data points to be able to compute the $d\theta/dz$. Since, the temperatures of the OH and O_2 layers are known, the temperature of OI 5577 was inferred from the SABER observation to calculate θ and then used to create a time series (which was kept constant) to attain the required needed input. Thus a constant time series of θ was created for the OI 5577 emission layer.

The zonal and meridional momentum fluxes of the gravity waves is determined by adapting the approach of Suzuki et al. (2007) and Vargas et al. (2009), given by,

$$\begin{aligned} M_{F\,zon} &= \rho_0\langle u'w'\rangle = -\rho_0\frac{1}{2}\frac{km\omega^2}{k_H^2}\frac{g^2}{N^4}\left(\frac{T'}{\overline{T}}\right)^2 \\ M_{F\,mer} &= \rho_0\langle v'w'\rangle = -\rho_0\frac{1}{2}\frac{lm\omega^2}{k_H^2}\frac{g^2}{N^4}\left(\frac{T'}{\overline{T}}\right)^2, \end{aligned} \tag{7}$$

where ρ_0 is the density at the emission layers, $k_H^2 = k^2 + l^2$ is the horizontal wavenumber with k and l being the zonal and meridional wavenumbers, m is the vertical wavenumber, ω is the intrinsic frequency, g is the gravitational acceleration and N the Brünt Väisälä frequency. The density, ρ_0 used in Equation 7 was obtained from SABER sounding close to the observation site during each GW event. The intrinsic frequency ω can be estimated from the expression, $\omega_0 - kU - lV$, where $\omega_0 = 2\pi/\tau$. U and V are the zonal and meridional wind speed in the direction of the wave, respectively, at each peak emission altitude. The horizontal wavenumber, k_H, was estimated from the horizontal wavelength, λ_H, estimated in the Equation A5 in Appendix A1, using the relation $k_H = 2\pi/\lambda_H$. The $T'/\overline{T}$ is the relative temperature perturbation, and T' is the GWs induced temperature variation, and $\overline{T}$ is the background temperature. The total momentum flux (M_F) of GW is given by (Vargas et al., 2007):

$$M_F = \rho_0 \langle u'w' \rangle = -\rho_0 \frac{1}{2} \frac{\omega^2}{k_H} \frac{g^2}{N^4} \left(\frac{T'}{\overline{T}} \right)^2, \tag{8}$$

Estimating the potential energy (E_p) and the momentum flux (M_F) of GWs depends on observed temperature and wind data. As mentioned earlier, rotational temperature from photometer observations were used for M_F and E_p.

3.5 All-Sky Image Pre-Processing and Spectral Analysis

To determine the horizontal parameters of the selected events, images from co-located all-sky imager at the São João do Cariri were used. The methodology used for all-sky images processing and GWs parameters estimation implores the validated and updated image pre-processing and spectral analysis (iPreSA) routine of Wrasse et al. (2024), which is capable of pre-processing original airglow images and in retrieving GWs characteristics. The pre-processing aspect includes; (a) the calibration of original images (i.e., to align the image to the geographic coordinates); (b) removal of stars to reduce their effect on the wave spectrum at high frequencies Maekawa (2000); (c) correction of the curvature effect of the charge-coupled device (CCD) camera by mapping the original images onto new coordinates that relate distances between pixels in the image to physical distances in the airglow layer with the zenith at the origin. Other minor corrections implemented in the pre-processing stage involve the estimation of intensity fluctuation fraction, application of high pass filter and weighting function. The current version of the pre-processing also incorporate the correction of Van Rhijn effect and atmospheric extinction, and removal of the milky-way Kubota et al. (2001); Wrasse et al. (2024).

The wave characteristics in the preprocessed airglow images will be obtained using a two-dimensional spectral analysis technique. The underlying concept of this technique is the two-dimensional Discrete Fourier Transform (2D-DFT), represented mathematically as

$$\mathcal{F}(k,l) = \sum_{x=0}^{m-1} \sum_{y=0}^{n-1} \left(c^{-i\frac{2\pi x k}{m}} \right) \left(c^{-i\frac{2\pi y l}{n}} \right) f(x,y) \tag{9}$$

where $\mathcal{F}$(k,l) is the Fourier transform of the function, k, l are the zonal and meridional wavenumbers and $m \times n$ is the dimension of the analyzed image. The cross-spectrum between two successive images is estimated from the amplitude and the phase of the waves. (λ_H), period (τ_H), phase speed (c_H), and propagation direction (ϕ_H). The step-by-step description of the

spectral analysis Wrasse et al. (2007), implemented to estimate the horizontal parameters of the observed GWs (Figueiredo et al., 2018; Wrasse et al., 2024) are presented in Appendix A1.

From the horizontal wavelength, the zonal (k) and meridional (l) wavelength numbers were determined and used in Equations 7 and 8 to estimate the momentum flux. An important condition considered in the selection of the horizontal propagating GWs is that the period must be equal or similar to the period of the vertical component observed in the photometer data. A summary of the keogram/spectral analysis and obtained result are shown in Figures A1, A2, A3, A4 and A5 in Appendix A1.

4 Results

The results of the two (2) selected cases obtained from Section 3 are presented in Figures 7 and 8. Events one (#01) and two (#02) respectively occurred on 04/12/2004 (4 December 2004) and 01/05/2005 (01 May 2005) at São João do Cariri are presented.

4.1 GW Event on 04 - 05/12/2004

In Figure 7, that is the 04/12/2004 GW event, the reconstructed GW oscillations (red solid line) using the observed periods determined in the OI, O_2, NaD and OH emission layers overplotted on the residual is presented in panel (a). The dominant periods used in the reconstruction of the waves in GW event #01 are 00.42 h (25.47 min) and 00.50 h (30.29 mins). The wave of $\tau = 25.47$ min was observed in all the four emission layers. For the second wave of this event, two similar periods, $\tau = 30.29$ min and $\tau = 33.47$ min were observed. The wave with $\tau = 30.29$ min, was detected in the IO, O_2 and NaD emission layers. However, the observed period in the OH was 0.55 h (33.47 min). Even though this period may differ from the period determined in the other emission layers, it deviation was not out of the error margin of the estimation and thus was considered. The error ranges were within $\pm$ 10% of the estimated periods. The consideration was based on the fact that this are observed observed periods which were determined under the influence of background wind.

In panel (b), the normalized residual of the reconstructed time series presented for each emission intensity and rotational temperature. The normalization is computed so as to standardize the range of variations in all the emission layers. From the normalized intensity variations, panel (c) was produced, from which the phases differences were determined. From the phase progression, an upward phase propagation, indicated by the first four black vertical dashed lines, was observed. For the two red dashed lines, a sharp upward phase propagation was observed between the four emission layers of OI, O_2, NaD and OH between 23:00 UT on 04/12/2004 and 01:30 UT on the 05/12/2004. Between the hours of 01:30 and 02:20 UT on the 05/12/2005, a steep upward phase propagation can be seen between OI, O_2 and NaD emission layers after which a downward phase propagation was then observed between NaD and OH. The turning point of the phase lines of the red dashed lines is highlighted by the light red background.

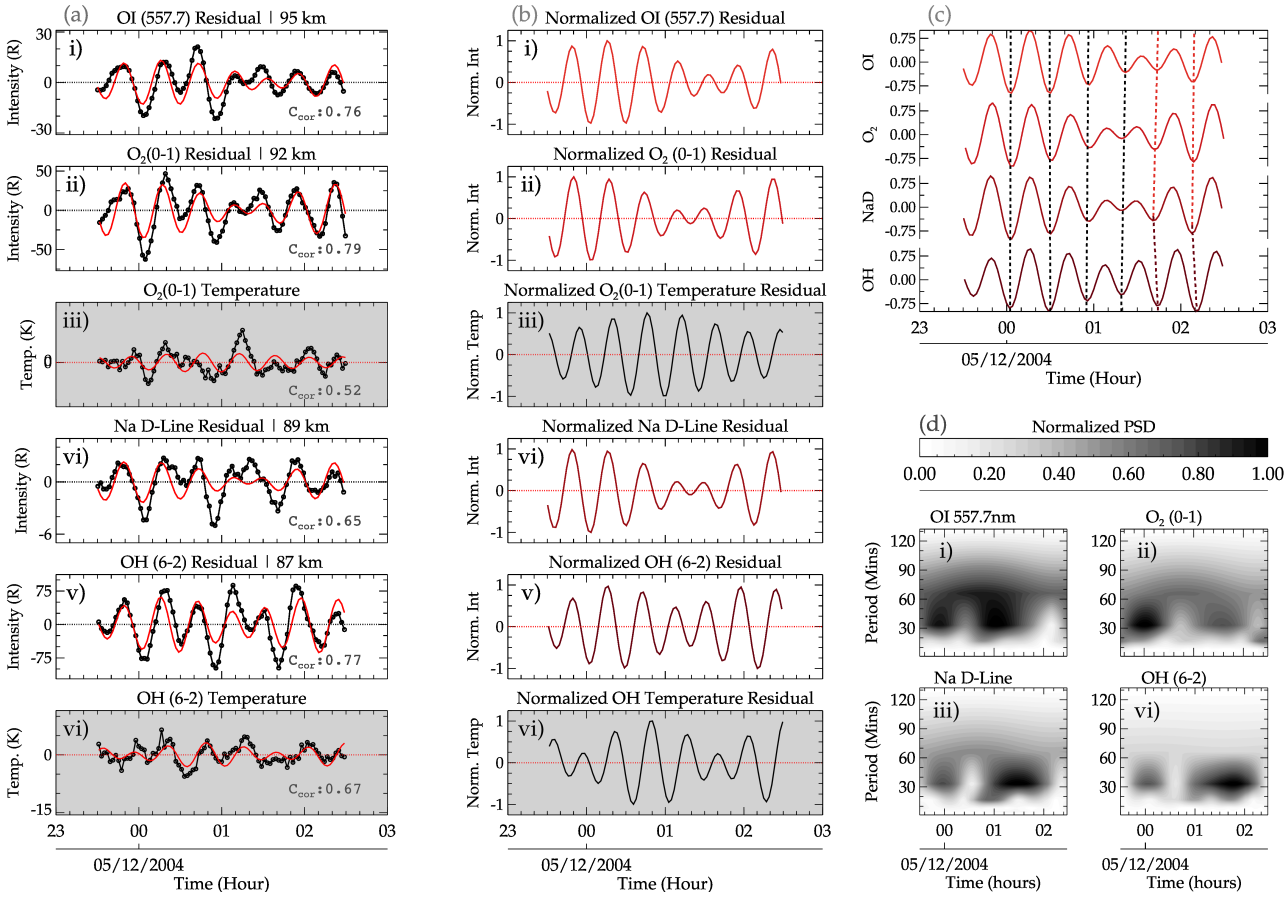

Figure 7. The detailed description of the processing stage of the preprocessed data (obtained form Figure 3). The reconstructed harmonics of the gravity wave oscillations (red solid line) using the dominant periods determined by Wavelet analysis and Lomb-Scargle periodogram, and the residuals for each airglow emission layer and the rotational temperature are presented in panel (a). The corresponding normalized residuals are shown in panel (b). Using the normalized residuals in panel (c), the phase propagation of the gravity wave oscillation at each emission layer altitude is determined using the vertical slanted dotted lines. In panel (d), the Wavelet analysis result of each emission layer is shown.

The observed periods estimated using Wavelet analysis is presented in Figure 7(d). It is observed that there is a strong presence of range of wave periods between 30 mins to 90 mins were observed in all the four (4) emission layers with dominant periods of 25.47 min (all emission layers), 30.29 min (for OI, O_2 and NaD) and 33.47 min (OH). These dominant periods were also present in the Lomb Scargle periodogram as shown in Figure 5. The plots in panel (d) are normalized to standardize the variations of the individual emission layers with the scale defined in the color bar.

Peak selection procedure considering the power spectral densities (PSD) were used to detect the significant periods. It is important to emphasize that GW event with the same periods / similar periods (within $\pm 5\%$ deviations) were chosen. The deviations were included in the choice of periods because they are observed period which are susceptible to the background

wind. The result on the estimated intrinsic parameters are presented and discussed in the later section. Using these periods and Equation 2, the signals (black solid line with open circle) for each emission layer is reconstructed (red solid line) as shown in panel (a) of Figure 7. Unlike Figure 3, the residuals of all the emission layers are plotted, including the rotational temperatures of OH and O_2. Similar to Figures 5 and 6, the rotational temperatures are presented in the plots with gray background in panels (a.iii) and (a.vi) of in Figure 7. In panels (b.i) - (b.vi) of Figure 7, the normalized reconstructed residual for each emission layer (including the rotational temperatures of OH and O_2) is presented.

From the reconstructed time series, a similarity can be seen in all the emission layers, which serve as an indication of similar GWs propagate through these layers. Even though similarities exist in the periodicities, some degree of variations can be seen. These variations can be attributed to the variations of the background wind, since the result obtained in the Lomb Scargle periodogram and the Wavelet are observed periods. It is worth mentioning that the time series of the rotational temperature has also been subjected to all the above mentioned procedures to confirm that similar wave observed in the intensity are also present in the temperature. In panel (c), the normalized reconstructed time series intensity is plotted in ascending order of altitude, from which the phase progression of the waves with altitude is determined. Using the dashed vertical lines, the phase progressions are determined.

4.2 GW Event on 01/05/2005

In Figure 8 (which is similar to Figure 7), panels (a), (b), (c) and (d) have the same arrangements. However, this event started at 18:00 UT to 23:30 UT on 1/05/2005. In all subpanels of panel (a), the reconstructed time series (red solid lines) using Equation 2 are plotted with the corresponding residuals of the airglow intensity variations as well as the O_2 and OH rotational temperature. To assess how best the reconstructed time series fits the residual, the cross correlation (C_{cor}) was estimated and presented in each subpanel of panel (a). In panel (b), the respective normalized intensities and rotational temperatures are presented.

The periods determined in each emission layer using a Wavelet analysis are presented in Figure 8(d). In subpanels (i), (ii), (iii) and (iv) of Figure 8(d), the spectrogram indicating the power spectral densities (PSD) relating the intensity of the periodicities of the wave to the time of occurrence for OI, O_2, NaD, and OH emission layers is presented. The PSD for all the airglow emission layers has been normalized. The scale of the variations is defined by the color bar. A broad spectrum of high PSD of the periods were observed extending from 30 to $\sim$90 min throughout the entire observation window with a peak centered around early hours of the observation, through the middle and the later time of the observation (especially for the OH emission.). The summary of the wave parameters of the photometers are presented in Table 3.

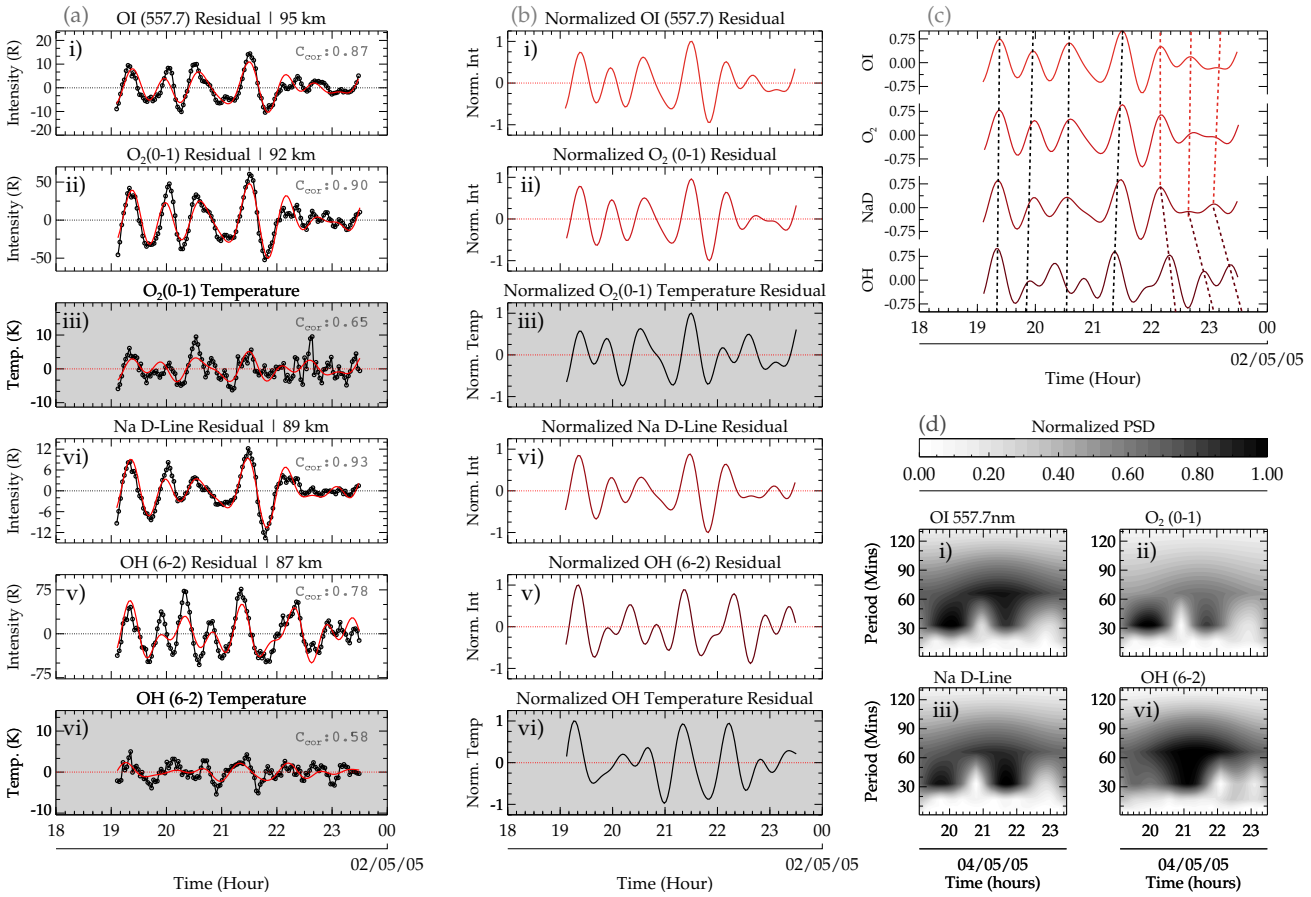

Figure 8. Same as Figure 7 but for 01/05/2005 GW event.

In panel (c) of Figure 8, the phase lines indicating the phase propagation across the four (4) emission layers are presented. Between the hours of 19:30 and ∼22:00 UT, a steep upward phase propagation extends from the OH through NaD and O_2 to the OI emission layers. After 22:00 UT till the 23:30 UT, the phase propagation was upward between the emission layers of NaD and OI, whereas between NaD and OH, phase propagation is down.

Table 3. Summary of the selected gravity waves events.

Events	Photometer			All-Sky Imager		Parameters	
	τ_z (min)	V_z (m/s)	λ_z (km)	τ_H(min)	λ_H (km)	M_F (m^2/s^2)	E_p (J/kg)
Event #01							
$\tau_1(O_2)$	25.47	inf	inf	23.10±1.20	91.00 ±6.30	01.07 × 10^{-2}	86.03
τ_1(OH)						01.09 × 10^{-2}	87.91
$\tau_2(O_2)$	33.47	05.28	10.60	33.60±1.70	135.41 ±11.59	01.07 × 10^{-2}	86.03
τ_2(OH)						01.09 × 10^{-2}	87.91
Event #02							
$\tau_1(O_2)$	31.64	62.84	119.31	28.90±1.40	255.90 ±17.60	04.50 × 10^{-2}	595.84
τ_1(OH)						00.46 × 10^{-2}	60.93
$\tau_2(O_2)$	43.25	108.08	280.50	46.20±2.30	237.00 ±14.40	02.72 × 10^{-2}	595.84
τ_2(OH)						00.28 × 10^{-2}	60.93
$\tau_3(O_2)$	58.43	11.64	40.80	61.03±3.10	454.40 ±26.20	02.72 × 10^{-2}	595.84
τ_3(OH)						00.28 × 10^{-2}	60.93

5 Discussion

5.1 Phase Propagation

As presented in Section 4, two events of similar periods were selected. For Event #01, two dominant periods were detected, however, estimated phase propagation associated with the first period indicates little or no phase change, implying it is possibly a ducted wave. For Event #02, the three dominant observed periods were determined. In Figure 9, the phase leads and lags between the four emissions layers are presented. This Figure is intended to determine by how much these GWs with similar period propagating through the emission layers lags or leads the preceding or succeeding layers using the phase shifts.

5.1.1 Event #01

From the phases of the GWs of Event #01, OH leads NaD by 8.60 min, whereas NaD leads O_2 by 1.21 min. O_2 lags OI by 3.25 min. A consistent phase lead can be observed from OH through NaD to O_2 except between O_2 and OI, where a phase lag was observed. The phase lag observed between the emission layers of O_2 and OI was induced by the background wind due to a shear. From the average wind between 23:30 and 02:30 UT in the direction of the wave, there exist a wind shear between 80 and 98 km as shown in Figure 9(c). This is suggestive of a phase shift of the waves. From Figure A2, a change in the direction from east to west above the OH emission layer in the zonal wind within the observation hour. Above the NaD emission layer

the zonal wind became predominantly westward and peaks in the O_2. Similarly, the meridional wind also exhibit a change a change in direction from north to south within the NaD layer during the time of the GW event. Despite this phase lag, the mean phase propagation of these GWs shows that OH leads OI by ∼06.58 min. Using this phase information and the period, Figure 9 is produced. These figures are used to evaluate the phases of the GWs in these two emission layers.

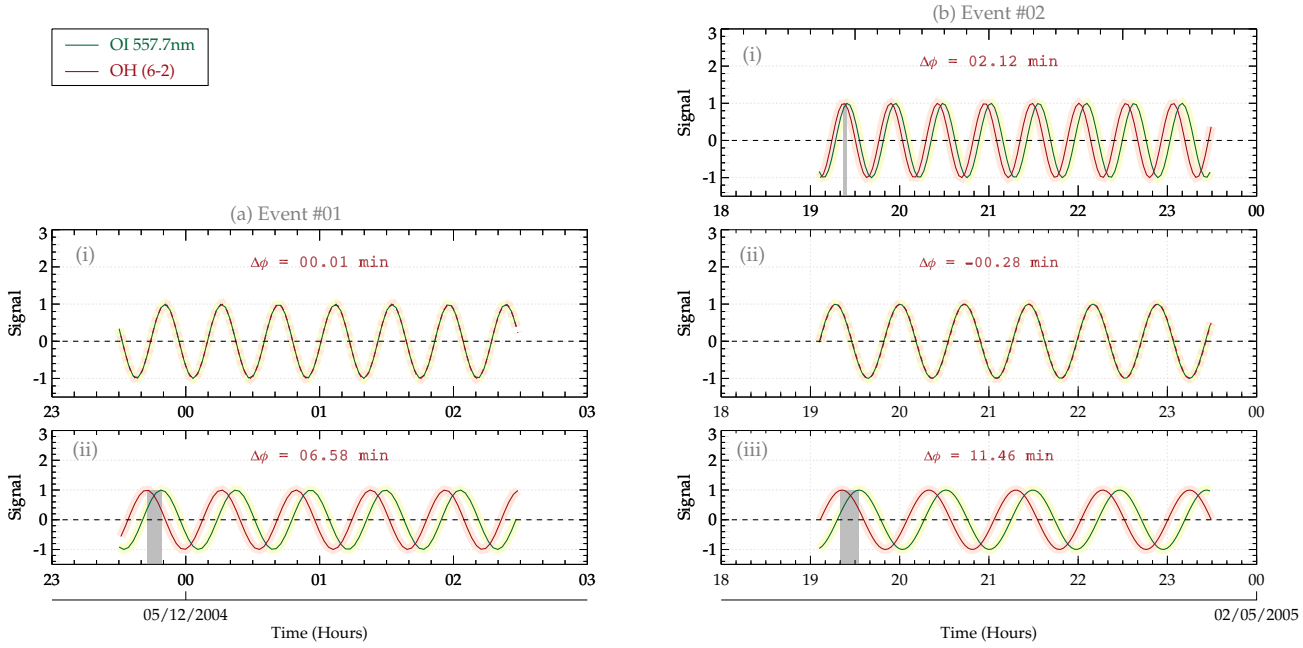

Figure 9. Two observed vertically propagating gravity wave (GW) events at São João do Cariri. In panel (a), the phase difference is determined using the reconstructed signal of O_2 and OH for Event #01. Using the reconstructed signal for each period in Event #02, the phase differences between O_2 and OH are determined and presented in panel (b).

In Figure 9, the reconstructed time series of GW events #01 and #02 are presented. In panel (a), the reconstructed time series of the GW of 04/12/2004 is shown. Subpanels (i) and (ii) show the reconstructed GWs of $\tau_1 = 25.47$ min and $\tau_2 = 33.47$ min, respectively. Based on the estimated phase difference ($\Delta\phi$) of 00.01 min of τ_1, the vertical velocity (V_z) and wavelength (λ_z) goes to infinity. This indicates very little or no phase difference. For τ_2 of GW event 01/05/2005, OH leads OI by $\Delta\phi$ =06.58 min. This phase difference led to V_z =05.28 m/s and λ_z =10.60 km. The summary of the estimation $\Delta\phi$, V_z, and λ_z for Events #01 and #02 are presented in Table 3.

5.1.2 Event #02

The phase propagation characteristics of GW event #02 (01/05/2005) is shown in Figure 9(b). The individual reconstructed GWs of each periods were constructed using the observation time of the data. In the subsequent subsections, the characteristics of the phase are discussed.

$\tau_z = 31.64$ min

For Event #02 (see Figure 6), propagation of the GW with $\tau = 31.64$ min shows a steep vertical downward phase propagation with altitude. Here, OH leads the NaD by 0.698 min (∼41.890 sec), NaD leads O_2 by 01.926 min, and O_2 lags OI by 00.502 min (∼30.136 sec). In general, OH leads OI of 00.0354 h (02.122 min). In comparison, Figure 9(b.i), a phase lead was observed between OH (red solid line) and OI (green dashed line) emission layers. In Figure 9(b(i)), the phase difference ($\Delta\phi$) between OH and OI is represented by a positive ($+$) value to indicate a lead.

$\tau_z = 43.25$ min

The second period ($\tau_z = 43.25$ min) of Event #02 demonstrated a a mixture of phase leads and lags in the phase propagation from OH through NaD and O_2 to OI emission layers, showing a steep vertical upward phase propagation for the first four (4) hours of the time series. No phase difference exists between OH and NaD, whereas NaD was found to leads O_2 by 0.00854 h (∼00.512 min / ∼30.748 sec). In the case of O_2 and OI, O_2 lags behind OI by 00.0132 h (∼00.793 min / ∼47.556 sec). Between OH and OI, OH lags OI by 0.00467 h (∼0.280 min / ∼16.808 sec). The phase propagation characteristics of this GWs is shown in subpanel (ii) of Figure 9(b). Here, the $\Delta\phi$ is negative due to the phase lag.

$\tau_z = 58.43$ min

The GW of period, $\tau_z = 58.43$ min, of Event #02 demonstrated a consistent phase leads from OH through NaD and O_2 to OI emission layers, indicating a vertical upward phase propagation between the four emission layers. The GW of this period indicates that OH leads NaD by 0.086 h (∼05.136 min), NaD leads O_2 by 0.0828 h (∼04.970 min) and O_2 leading OI by 0.0225 h (∼01.351 min). Generally, OH leads OI by 00.190 h (∼11.456 min). The phase propagation characteristics using the reconstructed time series of this GWs is presented in subpanel (iii) of Figure 9(b). The $\Delta\phi$ is positive due to the phase lead.

GWs propagation are used to determine the energy propagation (Nyassor et al., 2018, and references therein). A downward phase propagation indicate upward energy propagation and vice versa. In the case of Event #01, the phase across the four emission layers is upward and almost vertical; thus, the wave energy propagates almost vertically downward for some of the periods. The characteristics of both of these events are similar, except that, one of the period of GW in each event (i.e., τ_2 of Event #01 and τ_3 of Event #03) presented a well-defined vertical and upward phase propagation. The remaining period (as mentioned earlier) showed almost vertical phase lines between the emission layers due to the little or no phase difference, which causes V_z and λ_z to approach infinity (presented in Table 3).

The downward phase propagation indicates that this wave is generated upward and propagates downward (Vadas et al., 2018). Downward propagating GWs, just like upward propagating waves, transport momentum and energy from the source location, thus depositing this momenta and energies wherever they break or dissipate. However, these two cases presented three different dynamics:

1. almost vertical phase propagation across all emission layers;

2. an upward and downward phase propagation (fish bone structure) at the later hours of the observation times and;

3. out of phase variation of the O_2 and OH rotational temperatures at the later hours of the observation time.

These dynamics are discussed in details together the propagation conditions of the GWs across these emission layers as well as the characteristic of the momentum flux and potential energy.

5.2 Background Propagation Conditions

Due to the characteristics of the phase propagation of the two events considered in this study, the propagation conditions between 80 and 100 km were investigated. Figure 10 (a) and (b) represent the propagation conditions of GW events #01 and #02, respectively. In panels (a(i)) and (b(i)), the temperature profile obtained from SABER observation (solid line) and the estimated potential temperature (dashed lines) are presented. The potential temperature (θ) was estimated using Equation 6. The profile of the Brünt Väisäla frequency (N) presented in panels (a(ii) and (b(ii)) was estimated using Equation 5. The Brünt Väisäla frequency profile is mostly used to examine the formation of duct called thermal duct due to temperature gradient (Bageston et al., 2011). Ducts are known to trap vertical propagating GW, causing them to propagate horizontally for a longer distances and time.

Doppler duct, on the other hand, are caused by background wind gradient (Bageston et al., 2011; Isler et al., 1997). To determine whether or not the propagation of GWs are hindered or favored by the background conditions (controlled mainly by wind and temperature), the square of the vertical wavenumber (m^2) profile is used. The m^2 can be estimated using (Bageston et al., 2011):

$$m^2 = \left[\frac{N^2}{(u_0 - c)^2} - \frac{u_o''}{u_0 - c} - k_h^2\right] \tag{10}$$

where, N is the Brünt Väisäla frequency (N), u_0 is the observed horizontal wind in the direction of the wave propagtion, u_o'' is the second derivative of the wind with altitude, c is the observed phase speed, $k_h = 2\pi/\lambda_H$ is the horizontal wavenumber with λ_H being the horizontal wavelength. Equation 10 is a valid dispersion relation for gravity waves propagating in an environment where the effects of horizontal wind and temperature gradient cannot be neglected (Chimonas and Hines, 1986).

The profile of the horizontal wind in the direction of the wave propagation, $u_o = u\cos\psi + v\sin\psi$, is shown in panels (a(iii)) and (b(iii)) of Figure 10. Here, u and v are the zonal and meridional wind components, respectively, and ϕ is the propagation direction of the GW observed in the all-sky images. Using the other parameters defined in Equation 10, the m^2 profile is estimated and plotted panel (a(iv)) and (b(iv)).

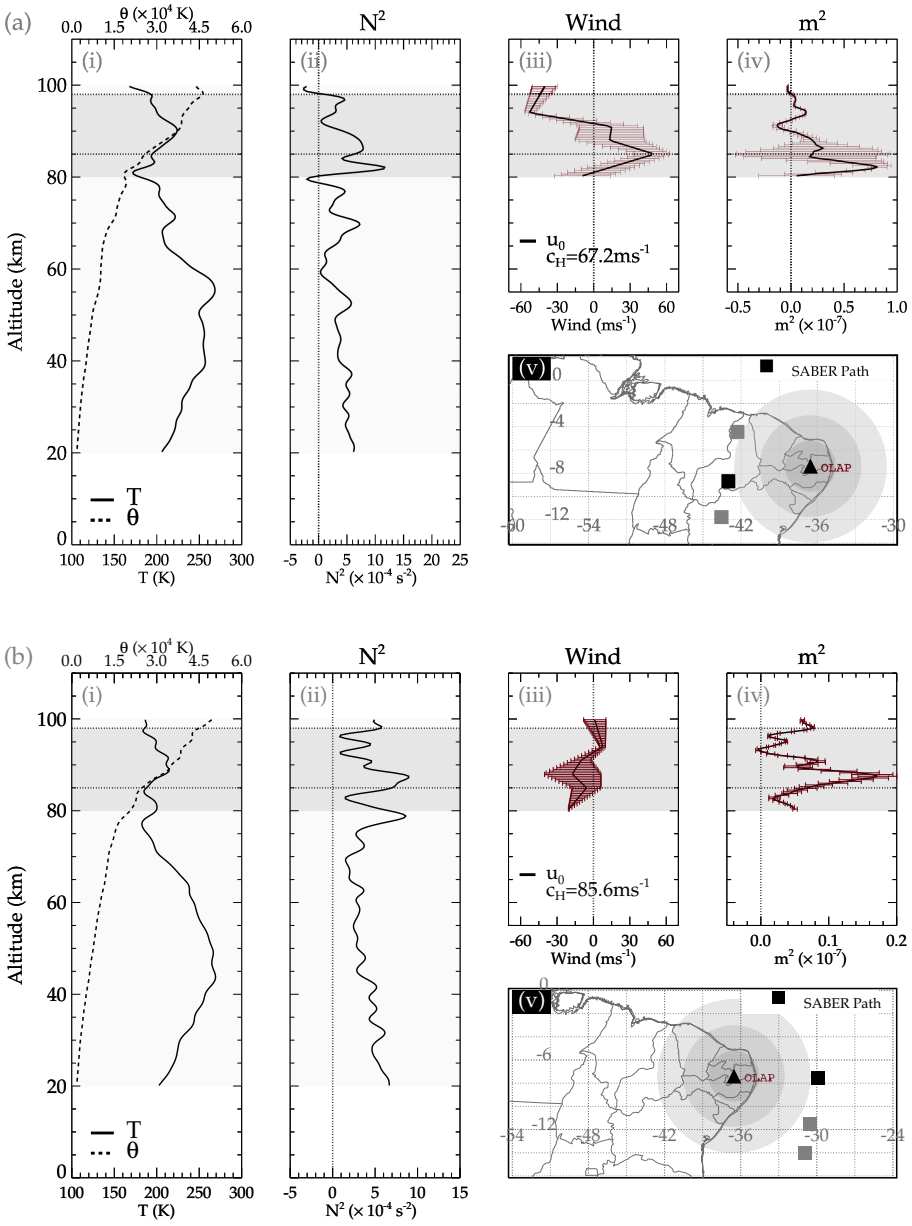

Figure 10. Propagation characteristics of the GW events observed on the 04 - 05/12/2004 (panel (a)) and 01 - 02/05/2005 (panel (b)) GW events. Kinetic temperature profile (i) of the selected SABER soundings (position of the profile of the black (v). The dashed line in (i) is the profile of the potential temperature. In (ii) the profile of Brünt Väisäla frequency is presented. In panels (iii) and (iV), the profile of the wind in the direction of the GW propagation and the m^2 are presented, respectively.

In panels (a(v)) and (b(v)), the geographical map of the OLAP facility and the sounding position of the SABER satellite are presented. The positions of the SABER sounding indicated by the squares, among which the temperature profile of the black square is selected for the computation of the potential temperature and the Brünt Väisäla frequency. The sounding positions during Event #01 started from -43.54°, -11.77° occurred at 00:47:29 UT through -43.00°, 08.70° at 00:48:30 UT to -42.28°, -04.45° at 00:49:41 UT. For Event #02, the sounding position started from -29.90°, -07.56° at 18:46:35 UT, -30.54° through -11.51° at 18:45:24 UT to -30.90°, -14.04° at 18:44:39 UT. These sounding positions and times fall within a defined radius of 800 km around the observation site. This radius was defined so that any sounding that fall within will be considered.

Several studies have demonstrated how the background conditions control the propagation characteristics of GWs. Using the m^2, the evanescent ($m^2 < 0$) and propagating ($m^2 > 0$) regions can be determined. Most ducts are formed when two evanescent regions exist above and below a region of $m^2 > 0$. From Figure 10, panels (a(iv)) and (b(iv)), shows the profiles of m^2 estimated using observed parameters. As mentioned earlier, ducts are formed when there is a gradient in the background temperature and wind. In both cases, a gradient can be observed in the temperature and wind (see the gray shaded region of each panels (i) and (ii)), indicating a possibility of a duct formation.

The m^2 profile, however showed structures of existence a ducted. During the GW event #01, two ducted region can be observed; the first one between ∼91 and 98 km and ∼80 and 90 km. The first duct encloses most likely the the peak altitudes of O_2 and OI emission layers. Even though this duct may appear quite weak, it is possible that has contributed to the trapping the GW within this emission layer. The second duct, which is stronger than the first, most likely favored the trapping of the GWs in the peak altitudes of OH and NaD emission layers. Despite the presence of the structure of duct, the GW phase propagation indicated a characteristic that appear to be an effect of a single duct. This is because, except a slight difference in the observed period of the τ_2 GWs of event #01 in the OH emission, all other emission have the periods (τ_2).

For the event #02, the structure of the duct presented almost the same characteristics as Event #01. An inversion layer could be observe in the temperature profile as shown in panel (b(i)). However, this inversion layer has not significantly influence the formation of the duct as shown in Figure 10(b(ii)). Only one observed evanescent region was formed at ∼94 km. Around 93 km, a quasi lower evanescent region can be seen. Even though the m^2 profile has a structure of a duct, only one evanescent region was formed. Besides this, the characteristics of the GWs observed in this event are similar to that of event #01. Considering the propagation dynamics of this waves, which is suggestive of the influence ducts, it is most probable that this structure might play an important role dynamics of the vertical propagation of this event.

5.3 Assessing the Duct Formation Contributing Factors

Formation of duct and its dynamics are mainly controlled by wind and temperature. These parameters are defined in Equation 10: (1) the buoyancy term, $N^2/(u_0 - c)^2$, resulting from the temperature and the curvature, $u''/(u_0 - c)$, term due to wind. To do this assessment, either the buoyancy term or the curvature term is ignored in Equation 10. Neglecting the curvature term, Figure 11(a(i)) shows a broad duct extending from ∼80 km to 98 km was form, with a maximum m^2 of $\sim 0.85 \times 10^{-7} \mathrm{m}^2$. Even though the lower part of the evanescent region is not well formed, it can be attributed to the limitation of the wind data to 80 km. Below 93 km the duct broadens to the lower (quasi) evanescent region extending down to 80 km. For event #01 and

considering only the curvature term (see Figure 11(a(ii))), two weak ducts were formed centered around 85 and 92 km with a maximum m^2 of 0.5×10^{-7}m^2 and 0.2×10^{-7}m^2, respectively.

The assessment for Event #02 presented in Figure 11(b). In the case where the curvature term was ignored (considering only buoyancy term), a duct with two maxima were formed between ∼80 and 93 km with a peak of $\sim0.18\times10^{-7}$m^2. Above ∼93 km, a narrow peak was also formed. Similar to the buoyancy term of Event #01, the lower limit of the evanescent region of this duct was not completely formed. Now, ignoring the buoyancy term as shown in Figure 11(a(i)) that the peak magnitude of the duct due to the curvature term is 0.04×10^{-7}m^2 (see panel (ii)). Two weak ducts were formed with peaks around 85 and ∼93 km, with a broad evanescent region extending from ∼87 to ∼92 km.

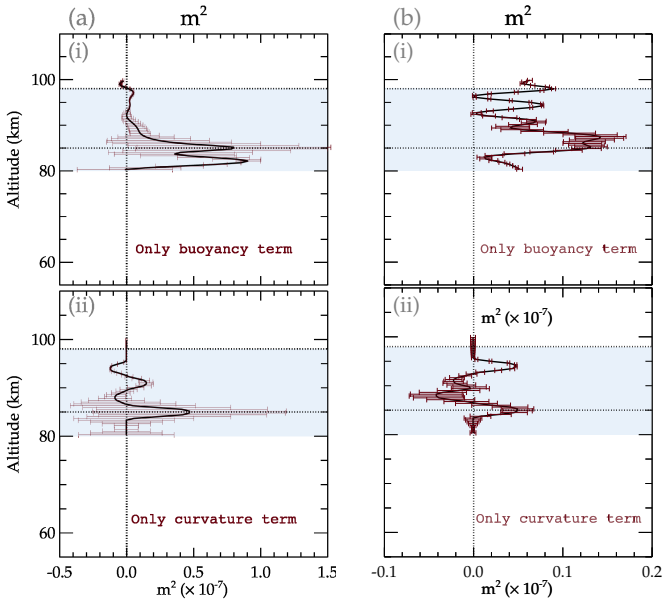

Figure 11. Assessing the influence of the buoyancy and curvature terms on the propagation characteristics of the GW events observed on the 04 – 05/12/2004 (panel (a)) and 01 - 02/05/2005 (panel (b)) GW events.

From Figures 5 and 11, it can be observed that there is a possibility of existence of ducts. These ducts are mainly due to temperature gradients. However, the ducts are considered weak (due to low m^2 values) and also having multiple ducts with some not having a well form evanescent regions ($m^2 < 0$). The observed ducts in this work can be said not to give the entire structural dynamics because the sounding positions during the GW events are quite distant from the observation site. From the phase lines little or no phase difference were observe during the first two hours of Event #01 and approximately the first three hours of Event #02. Using the phase difference, except for a period in each event, the estimated vertical wavelength (λ_z) approaches infinity thus vertical wavenumber ($m \to 0$). This characteristics causes the wave to undergo total internal reflection (Gossard and Hooke, 1975). Due to the limitation of the photometer airglow observations, the full extent of the dynamics cannot be explored. This will be explored in a companion paper.

5.4 Fish borne Structure and Out-of-Phase Temperature Variation

Figures 5 and 6, show an upward and a downward phase progression, forming a fish borne structure described in the work of Vadas et al. (2018). In their work, the authors applied a procedure to explore whether or not the turning points in both cases (which occurred around the NaD emission layer) is a reflection point or a region where dissipation occurred and possible excitation of other spectrum of GWs. It is known that for GWs to be considered as non-primary waves as shown by various works (e.g, Vadas et al., 2003, 2018; Kogure et al., 2020; Heale et al., 2020), the GW propagation characteristics for the upward and downward components must be different. The events considered in this work presents GWs with same period propagating through the NaD, O_2, and OI emission layers were observed except for OH which differs slight but fell within the error margin. This shift in the period could not be account for using the profile of the wind in the GW propagation direction in Figures 5(a and b).

Despite there is no existing evidence in the m^2 profile to explain the fish borne structure, the rotational temperature variation of the OH showed a shift and eventually got out of phase with the O_2 rotational temperature and the remaining emission layers (see Figure 4). This characteristics had been reported by Takahashi et al. (1998, and references therein) to be due to reflected GWs. Therefore, considering the fact that the OH rotational temperature is out of phase with O_2 and the remaining emission intensity variation at the later times of the observation or usable window of the data considered in this, indicate the possibility of reflection.

6 Momentum Flux and GW Potential Energy

Gravity waves transport momentum and energy from their excitation/source location to their sink (dissipation/breaking), whether the waves are upward or downward propagating (Fritts and Alexander, 2003; Vadas et al., 2009; Nyassor et al., 2021). The amplitude of upward propagating GWs grows due to the decreasing density with increasing altitude. So, for a downward propagating wave, the amplitude of the wave may suffer amplitude decrease due to increasing density with decreasing altitude. In Section 5.1, two GW events are selected with an upward phase propagation. The phases analysis in Figure 6 further showed phase leads and also small phase shifts. The individual reconstructed signal using the wave phases and periods affirms there exist phase difference between OI and OH emission layers.

According to Vadas (2007), diffusion processes inhibit the propagation of GWs where molecular viscosity and thermal diffusivity are significant in the upper mesosphere and lower thermosphere. Eddy diffusion is also known as a significant process that inhibits gravity wave propagation in the lower and middle atmosphere (Yiğit and Medvedev, 2016). However, high-frequency GWs mostly survive these conditions and are capable of propagating to the upper atmosphere, where they break or dissipate. However, what will be the characteristics of GWs momentum flux and potential energy for either an upward or downward propagating gravity wave, when they happen to be in a duct? These features are calculated from the momentum flux and potential energy of the GWs detected in the O_2 and OH emission layers, using their rotational temperature.

6.1 GW Event #01

The momentum and energy variation with time (and averages) at the O_2 and OH emission is presented in Figure 12 for the GW event of 04/12/2004 (event #01). Note that the same/similar period GWs determined in the variation of intensity of the four emission layers were determined in the rotational temperatures of the O_2 and OH. In Figure 12(a, b, c, d), background temperature, residual, potential temperature and Brünt Väisäla frequency time series are presented.

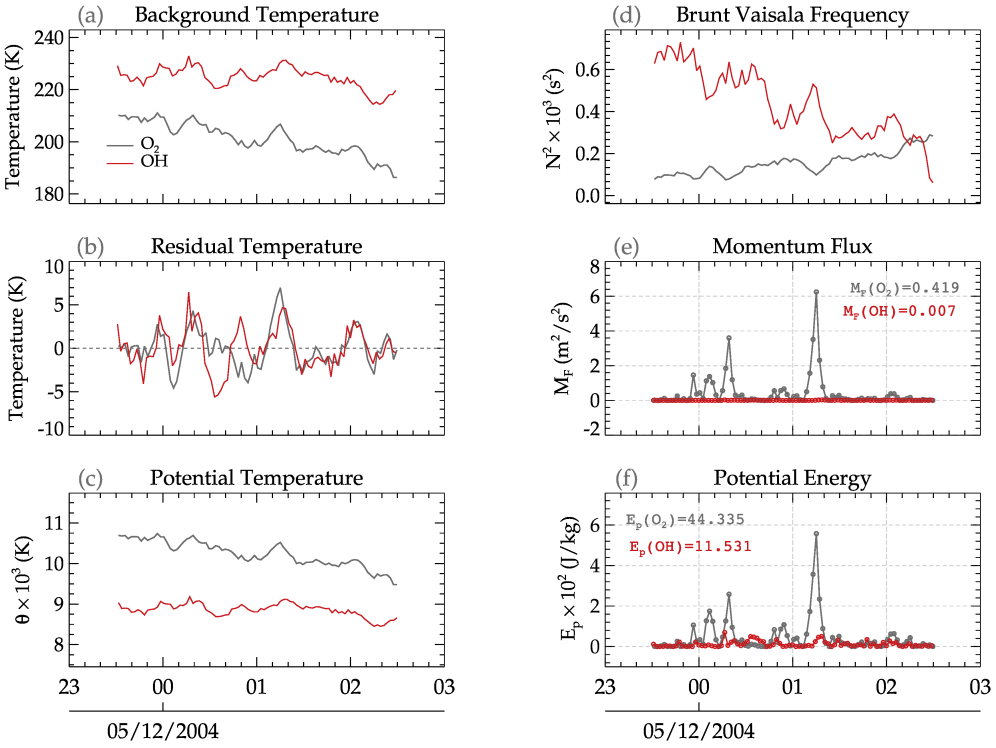

Figure 12. The characteristics of momentum flux (e) and potential energy (f) at the O_2 and OH emission altitudes for the event of 04/12/2004. In panels (a), (b), (c), (d)), background temperature, residual temperature, potential temperature and Brünt Väisäla frequency time series are presented, respectively.

The black solid lines represent the time series of the O_2, whereas the red line indicate the OH time series. The estimated momentum flux at the peak altitudes of O_2 (92 km) emission layer and OH (87 km) emission layer is shown in panel (e). The time averages of the momentum fluxes for O_2 and OH indicated that the momentum flux of the GW in the O_2 ($M_{F(O_2)}$) is greater than the momentum flux in the OH emission layer ($M_{F(OH)}$). Similarly, the potential energy (E_p) in the O_2 is higher compared to that of OH.

6.2 GW Event #02

Similar to Event #01, the background temperature, residual, potential temperature and Brünt Väisäla frequency time series are presented panels (a), (b), (c) and (d) of Figure 13. The momentum flux and potential energy at each emission layer for the three GWs observed in the event of 01/05/2005 is presented in panels (e) and (f).

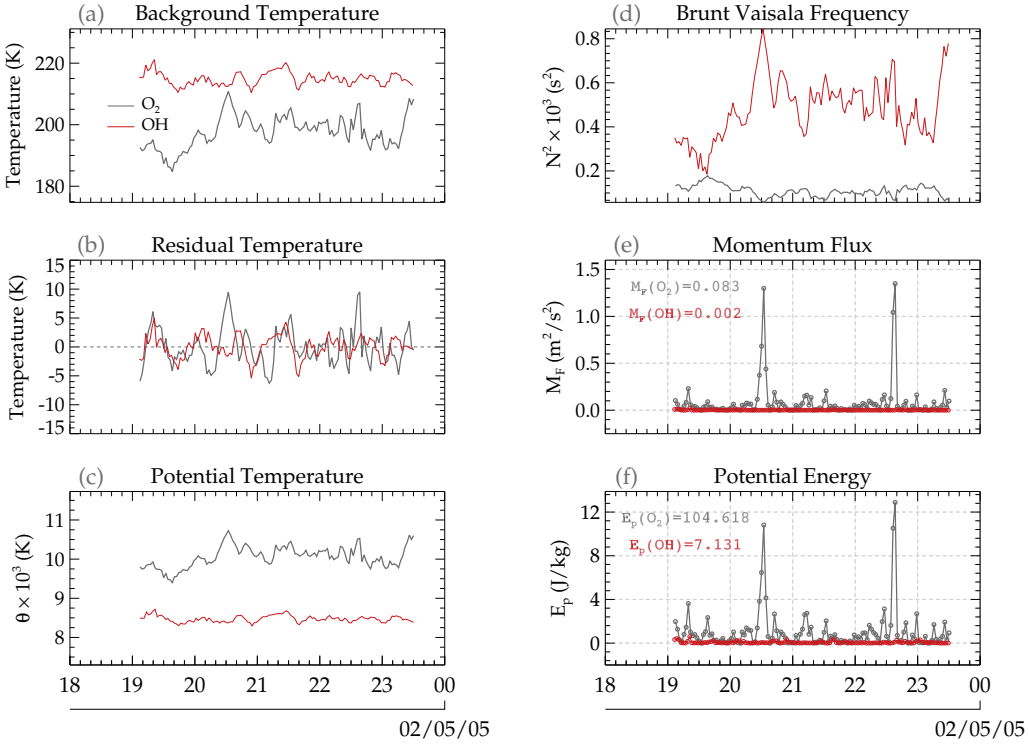

Figure 13. The characteristics of momentum flux (e) and potential energy (f) at the O_2 and OH emission altitudes for the event of 01/05/2005. In panels (a), (b), (c), (d)), background temperature, residual temperature, potential temperature and Brünt Väisäla frequency time series are presented, respectively.

Comparison between the momentum fluxes at O_2 and OH emission layers for this event showed a vast difference in the momentum fluxes. The M_F at the O_2 is much higher than at OH. This difference is attributed to the large amplitude of the gravity wave perturbations in the O_2 temperature residual since the estimation of the potential energy and the momentum flux depend on the temperature residual. However, for the GW event of 04 - 05/12/2004, the amplitude of the temperature perturbations due to GWs are similar. What made the momentum flux greater in the O_2 altitude is the spikes. Besides these spikes, the momentum flux at the O_2 and OH altitudes are similar. Another explanation for this difference apart from the increase in amplitude due to a decrease in density with altitude, is N^2. The times series of the N^2 varied considerably over the observation window, especially in the OH emission layer for both events.

Comparison between the two events showed that regardless of the vertical propagation of GWs, momentum and energy are transported from the source to the sink. It is imperative to say that the momentum and energy at the source will be less. This has clearly been demonstrated in these two selected events, attesting to the fact that atmospheric density significantly impacts the amplitude, momentum, and energy. Using Lidar temperature profile, Kaifler et al. (2017) studied the dynamics of downward propagating gravity waves. They observed that one third of the momentum flux is carried by the downward propagating GW from 85 km altitude to a lower altitude. In this work, this characteristics could not be accounted for due to the presence of ducts which could possibly change the dynamics of momentum and energy transportation. In general, the momentum flux and potential temperature for both events are higher in the O_2 emission layer than that of OH. It can be postulated that if indeed a duct exists in each events between, then the momentum and potential energy should be higher in the peak region of the duct, where O_2 is situated. At the reflection points (where $m^2 < 0$), the momentum flux and the potential energy should be less. This postulate could not be explored due to lack of high vertical observations between 80 - 100 km. This subject is however intended to be examined in a companion paper.

Considering the fact that the vertical propagation of these GWs are only within a 5 km range, the full extent of the characteristics cannot be explored due to the data set being unavailable. The potential energy of Event #01 also depicted characteristics similar to the momentum flux. Lesser momentum flux and potential energy on the OH emission layer is indicative of no deposition of momentum and energy, whereas higher in the O_2 is a pointer to deposition. Thus, it illustrates the governing theory of the transport of momentum and energy by atmospheric GWs. Using a longer altitude range and high temporal resolution lidar data, for instance, this subject can be explored in detail, and standards can be defined to determine the signatures of vertical propagating GWs due to reflection and non-primary GWs.

7 Conclusions

This paper studies the dynamic characteristics of momentum flux and potential energy of vertical (almost downward) propagating GWs using two GW events selected for case study. Using the phase propagation of GWs with almost the same period through the emission layers of OI 5577, O_2, NaD, and OH, the vertical propagation of the waves was determined. Using the ratio of the altitude difference (Δd) to the phase difference ($\Delta \phi$), the vertical phase speed and, consequently, the vertical wavelength were estimated. From the phase propagation, two classical events each of almost a downward propagating GWs was selected for further studies.

The potential energy and momentum flux were estimated, and their characteristics were studied. For each propagating GWs, it was determined that the momentum flux and potential energy at the O_2 emission altitudes were higher than those at OH emission altitudes. The momentum flux and the potential energy at the OH emission altitude are far lower than that of the momentum flux at the O_2 emission layer. No distinct amplitude enhancement of GW were observed in the O_2 as compared to GW observed in the OH emission layer. The similar GW amplitude of propagating wave in the O_2 and OH rotational temperature indicates a restricted or bounded propagation condition.

Due to the steep phase difference between the four emission layers, background propagation conditions are investigated. The m^2 profile suggested the presence of a ducts during thee two events. These ducts were found to be created due to temperature inversion. There is no idea about the full extent and dynamics of the ducts because the SABER sounding positions from which the temperature profile are distant from the observation sites. However, due to the dynamics of $m \to 0$ caused by steep phase line suggesting total reflection, indicates the presence of ducts. The presences of the duct is further confirmed by the no amplitude difference between the two emission layers.

It was observed that getting to the end of the observation/time series, the OH rotational temperature was out-of-phase with respect the intensity variations of OI, O_2, NaD and OH as well as the OH and O_2 rotational temperature. This kind of characteristics is caused by reflection of GW. The observed duct could not be used to support explain why the OH rotational temperature was out-of-phase. The fish borne structure formed at the end of the observation time typically is suggestive of a reflection.

As mentioned earlier in this work, the altitudes difference of the two rotational temperatures, is limited to only a 5 km, that is, only in the mesopause region. Hence, to come to a definite conclusion whether or not the steep phase lines, high λ_z and same/similar GW amplitude (residual temperature) are due to the imposing propagation restriction by duct, a detailed and companion study is intended to be conducted using Lidar data and other co-located observations. However, this work demonstrated that momentum and energy deposition are affected in the presence of a duct.

Appendix A: Retrieval of Gravity Wave Parameters from OH all-sky Images and Meteor Radar Wind Dynamics.

A1 Spectral and Keogram Analysis

In order to extract the parameters of gravity waves, a discrete Fourier transform based spectral analysis was used. First, a region containing GW oscillations were selected in both zonal and meridional component of the keogram components, as shown in Figure A1. Note that the same area in each of the components were considered for analysis. Next, a discrete Fourier transform (Equation A1) is applied to the selected areas (Wrasse et al., 2007; Figueiredo et al., 2018).

$$F(\omega) = \sum_{n-0}^{N-1} f(t) e^{\frac{-2\pi\omega n_i}{N}} \tag{A1}$$

in which $F(\omega)$ is the transform of the Fourier function $f(t), \omega = 0, ..., N-1$ is the frequency index, and N is the number of points in time series within the selected regions. Then, the cross spectrum defined by

$$C(x) = F_s(\omega) F^*_{s+1}(\omega) \tag{A2}$$

in which $C(\omega)$ is the cross spectrum between two time series and $F_s(\omega)$ and $F^*_{s+1}(\omega)$ represent the Fourier transform of the series $f_S(t)$ and $f_{s+1}(t)$, respectively. $F^*_{s+1}(\omega)$ is the complex conjugate of $F_{s+1}(\omega)$. The one-dimensional cross power spectrum is defined by the quadratic modulus, $|C2|$. The amplitude of the cross power spectrum is then determined using $2\sqrt{|C^2|}$, with the phase of the cross spectrum defined by

$$\Delta\psi = tan^{-1}\left\{\frac{Im(C(\omega))}{Re(C(\omega))}\right\}, -\pi \leq \psi \geq \pi. \tag{A3}$$

The phase difference between these time series caused by the wave propagation is considered to be the frequency ω, corresponding to the maximum amplitude. From the above estimations, the wave parameters are determined as follows:

1. Period (min):

$$\tau = \frac{1}{|f(\omega)|}; \tag{A4}$$

2. Horizontal wavelength (km):

$$\lambda_H = \frac{\lambda_{NS}\lambda_{EW}}{\sqrt{\lambda_{NS} + \lambda_{EW}}}, \tag{A5}$$

where, wavelength (km) for the zonal and meridional components $(\lambda_{NS}, \lambda_{EW})$ is $\lambda_{NS,EW} = \frac{\Delta d}{\Delta\psi/360^\circ}$, in which Δd is the distance between the time series.

605 3. The horizontal phase velocity $C_H(m/s)$, and phase propagation direction $\phi(^\circ)$, are determined by

$$c_H = \frac{\lambda_H}{\tau} \quad \text{and} \quad \phi = cos^{-1}\left(\frac{\lambda_H}{\lambda_{NS}}\right). \tag{A6}$$

Five GWs were detected from these two events using the above described spectral analysis. These results are presented below.

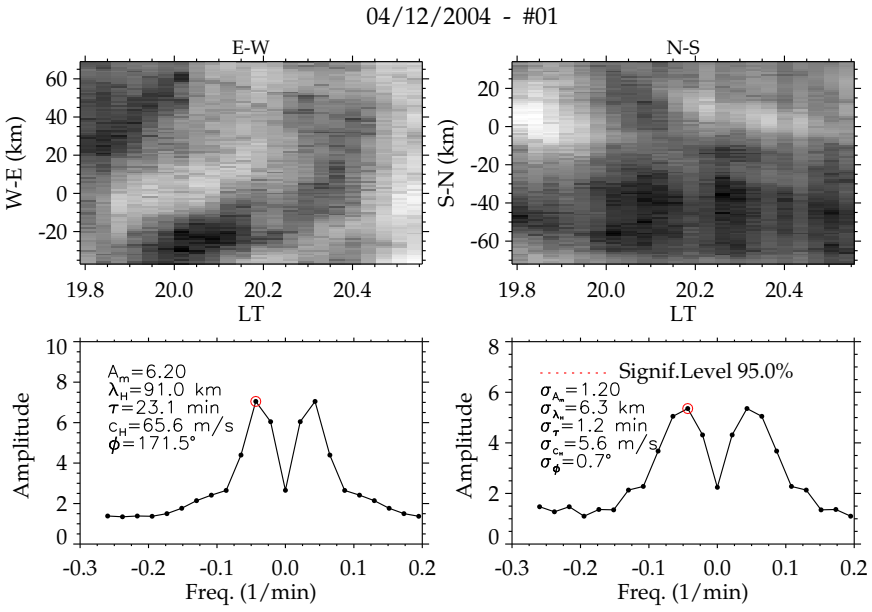

Figure A1. Result of OH emission layer keogram/spectral analysis of Event #01 with period, $\tau = 23.10$ min.

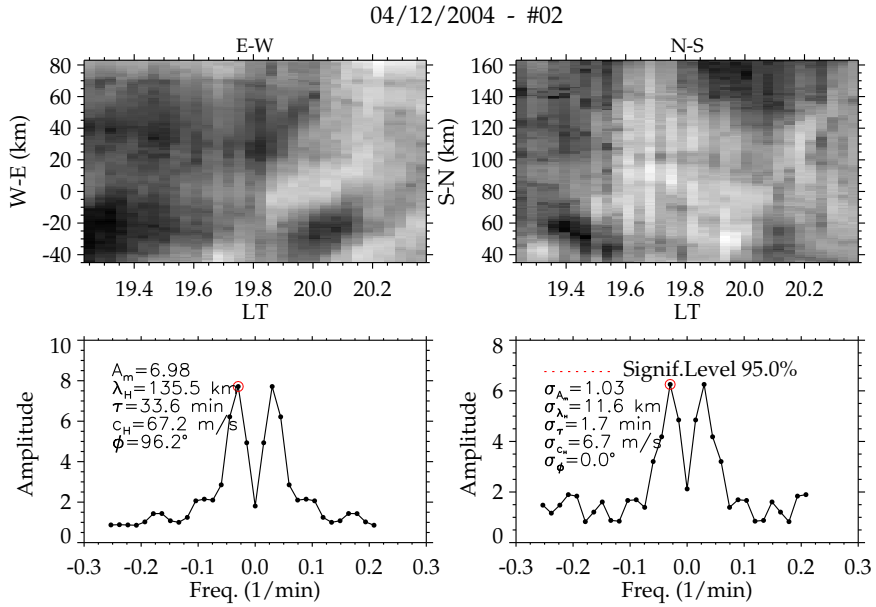

Figure A2. Result of OH emission layer keogram/spectral analysis of Event #01 with period of $\tau = 33.60$ min.

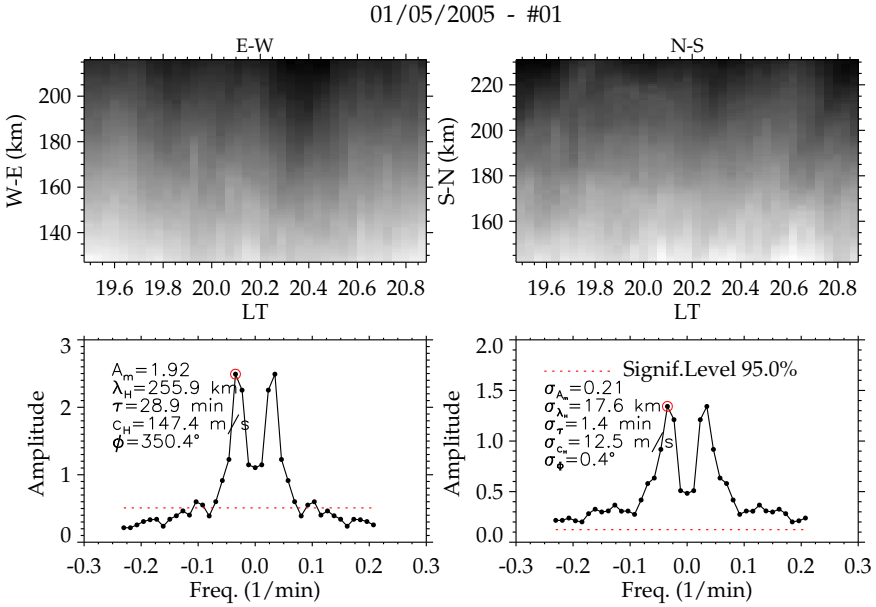

Figure A3. Result of OH emission layer keogram/spectral analysis of Event #02 with period of $\tau = 28.90$ min

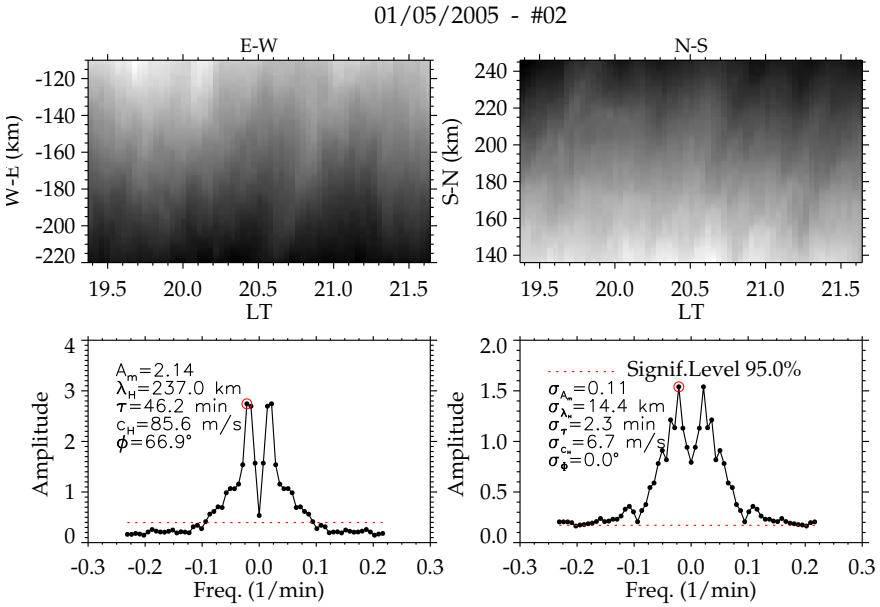

Figure A4. Result of OH emission layer keogram/spectral analysis of Event #02 with period of $\tau = 46.20$ min

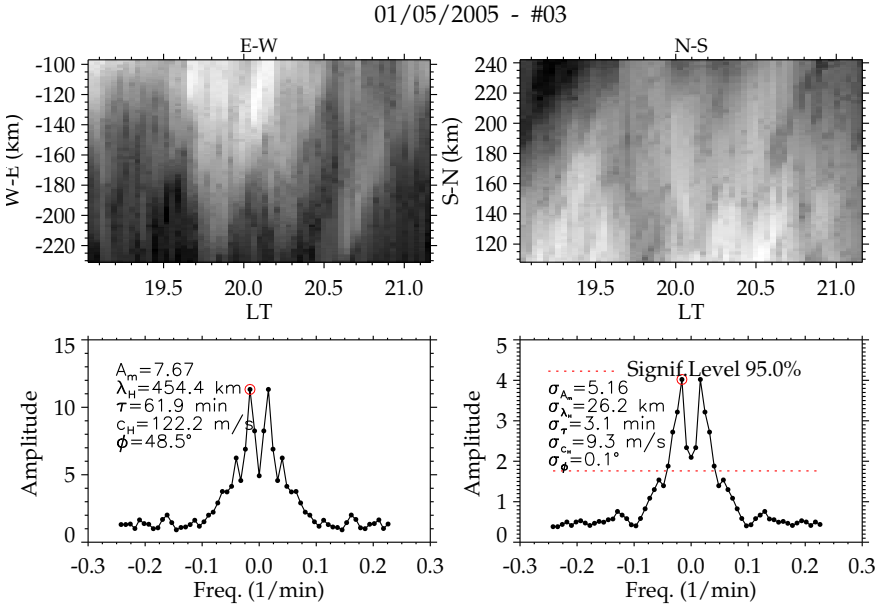

Figure A5. Result of OH emission layer keogram/spectral analysis of Event #02 with period of $\tau = 61.90$ min

In the upper panel, (the left side) is the zonal keogram, whereas the right side is the meridional (merid) keogram. These keograms correspond to the selected region with GWs perturbations. The lower panel is the amplitude (left) with the GW

parameters listed and their corresponding standard deviation (σ) in the middle right panel. The red dotted horizontal lines indicate a significant level greater than 95.0%, whereas the red circle with a black dot shows the peak amplitude. The GW characteristics in the lower panel are the horizontal parameters (i.e., the sum of the zonal and meridional components).

A2 Observed horizontal wind during the gravity wave events

In Figure A6 and A7, the zonal and meridional winds are presented in panels (a) and (b) are presented.

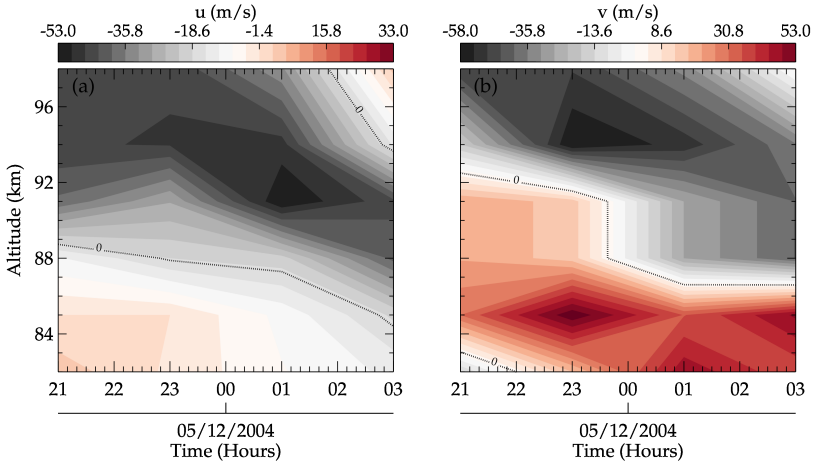

Figure A6. Meteor radar winds during the 04/12/2004 gravity wave (GW) event at São João do Cariri. The zonal and meridional winds are presented in the panels (a) and (b).

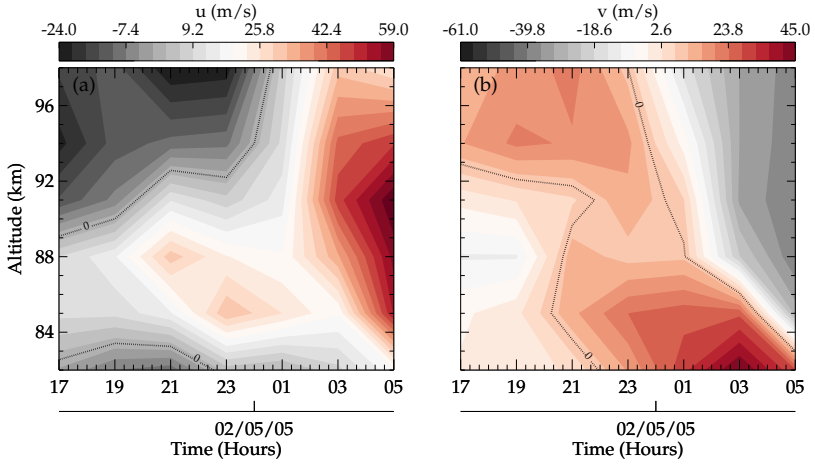

Figure A7. Same as Figure A1 but for 01/05/2005, 2005 gravity wave (GW) event at São João do Cariri.

Author contributions. PKN wrote the article and performed most of the analysis. CMW assisted in the validation of the methodologies and in the revision of the manuscript. IP assisted in the validation of the some methodologies and in the revision of the manuscript. EY assisted in the validation of the methodology and revision of the manuscript. CAOBF assisted in the development and validation of some of the methodologies and the revision of the manuscript. RAB provided the photometer an meteor radar data. FE processed the meteor radar wind data an revised the manuscript. HT revised the manuscript, and GAG helped in the validation of some of the methodologies and the revision of the manuscript. OMA revision the manuscript.

Competing interests. The contact author has declared that none of the authors has any competing interests.

Acknowledgements. Prosper K. Nyassor acknowledge the support of Fundação de Amparo à Pesquisa do Estado de São Paulo (FAPESP). The authors also thank the Coordenação de Aperfeiçoamento de Pessoal de Nível Superior (CAPES) and the Conselho Nacional de Desenvolvimento Científico e Tecnológico (CNPq) for the support. Thanks are given to the Brazilian Ministry of Science, Technology and Innovations (MCTI) and the Brazilian Space Agency (AEB). Cosme A. O. B. Figueiredo acknowledges FAPESP and the Fundação de apoio à pesquisa do estado da Paraíba. The authors thank the Estudo e Monitoramento Brasileiro do Clima Espacial (EMBRACE/INPE) for the provision of all-sky.

References

Bageston, J., Wrasse, C. M., Batista, P., Hibbins, R., Fritts, D., Gobbi, D., and Andrioli, V.: Observation of a mesospheric front in a thermal-doppler duct over King George Island, Antarctica, https://doi.org/10.5194/acp-11-12137-2011, 2011.

Becker, E. and Schmitz, G.: Climatological Effects of Orography and Land–Sea Heating Contrasts on the Gravity Wave–Driven Circulation of the Mesosphere, Journal of the Atmospheric Sciences, 60, 103 – 118, https://doi.org/10.1175/1520-0469(2003)060<0103:CEOOAL>2.0.CO;2, 2003.

Bowman, K. P.: An Introduction to Programming with IDL: Interactive data language, Elsevier, 2006.

Buriti, R., Takahashi, H., and Gobbi, D.: First results from mesospheric airglow observations at 7.5 º S., Revista Brasileira de Geofísica, 19, 169–176, 2001.

Chimonas, G. and Hines, C.: Doppler ducting of atmospheric gravity waves, Journal of Geophysical Research: Atmospheres, 91, 1219–1230, 1986.

Chou, M. Y., Lin, C. C., Yue, J., Tsai, H. F., Sun, Y. Y., Liu, J. Y., and Chen, C. H.: Concentric traveling ionosphere disturbances triggered by Super Typhoon Meranti (2016), Geophysical Research Letters, 44, 1219–1226, https://doi.org/doi:10.1002/2016GL072205, 2017.

Figueiredo, C., Takahashi, H., Wrasse, C., Otsuka, Y., Shiokawa, K., and Barros, D.: Investigation of nighttime MSTIDS observed by optical thermosphere imagers at low latitudes: Morphology, propagation direction, and wind filtering, Journal of Geophysical Research: Space Physics, 123, 7843–7857, https://doi.org/https://doi.org/10.1029/2018JA02543, 2018.

Figueiredo, C., Vadas, S., Becker, E., Wrasse, C., Takahashi, H., Nyassor, P., and Barros, D.: Secondary gravity waves from the Tonga volcano eruption: Observation and modeling over New Zealand and Australia, Journal of Geophysical Research: Space Physics, 128, e2023JA031 476, 2023.

Fritts, D. C. and Alexander, M. J.: Gravity wave dynamics and effects in the middle atmosphere, Reviews of geophysics, 41, https://doi.org/10.1029/2001RG000106, 2003.

Gossard, E. E. and Hooke, W. H.: Waves in the atmosphere: atmospheric infrasound and gravity waves-their generation and propagation, Atmospheric Science, 2, 1975.

Heale, C. and Snively, J.: Gravity wave propagation through a vertically and horizontally inhomogeneous background wind, Journal of Geophysical Research: Atmospheres, 120, 5931–5950, https://doi.org/10.1002/2015JD023505, 2015.

Heale, C. J., Bossert, K., Vadas, S. L., Hoffmann, L., Dörnbrack, A., Stober, G., Snively, J., and Jacobi, C.: Secondary gravity waves generated by breaking mountain waves over Europe, Journal of Geophysical Research: Atmospheres, 125, e2019JD031 662, https://doi.org/10.1029/2019JD031662, 2020.

Holton, J. R.: The role of gravity wave induced drag and diffusion in the momentum budget of the mesosphere, Journal of Atmospheric Sciences, 39, 791–799, https://doi.org/10.1175/1520-0469(1982)039<0791:TROGWI>2.0.CO;2, 1982.

Innis, J. L., Phillips, F. A., Burns, G. B., Greet, P. A., French, W. J. R., and Dyson, P. L.: Mesospheric temperatures from observations of the hydroxyl (6–2) emission above Davis, Antarctica: A comparison of rotational and Doppler measurements, Annales Geophysicae, 19, 359–365, https://doi.org/10.5194/angeo-19-359-2001, 2001.

Isler, J. R., Taylor, M. J., and Fritts, D. C.: Observational evidence of wave ducting and evanescence in the mesosphere, Journal of Geophysical Research: Atmospheres, 102, 26 301–26 313, 1997.

Kaifler, N., Kaifler, B., Ehard, B., Gisinger, S., Dörnbrack, A., Rapp, M., Kivi, R., Kozlovsky, A., Lester, M., and Liley, B.: Observational indications of downward-propagating gravity waves in middle atmosphere lidar data, Journal of Atmospheric and Solar-Terrestrial Physics, 162, 16–27, 2017.

Kogure, M., Yue, J., Nakamura, T., Hoffmann, L., Vadas, S. L., Tomikawa, Y., Ejiri, M. K., and Janches, D.: First Direct Observational Evidence for Secondary Gravity Waves Generated by Mountain Waves Over the Andes, Geophysical Research Letters, 47, e2020GL088 845, https://doi.org/10.1029/2020GL088845, 2020.

Kubota, M., Fukunishi, H., and Okano, S.: Characteristics of medium-and large-scale TIDs over Japan derived from OI 630-nm nightglow observation, Earth, planets and space, 53, 741–751, 2001.

Le Du, T., Keckhut, P., Hauchecorne, A., and Simoneau, P.: Observation of gravity wave vertical propagation through a mesospheric inversion layer, Atmosphere, 13, 1003, https://doi.org/10.3390/atmos13071003, 2022.

Li, Q., Xu, J., Liu, H., Liu, X., and Yuan, W.: How do gravity waves triggered by a typhoon propagate from the troposphere to the upper atmosphere?, Atmospheric Chemistry and Physics, 22, 12 077–12 091, https://doi.org/10.5194/acp-22-12077-2022, 2022.

Lima, L., Batista, P., Takahashi, H., and Clemesha, B.: Quasi-two-day wave observed by meteor radar at 22.7 S, Journal of atmospheric and solar-terrestrial physics, 66, 529–537, 2004.

Lindzen, R.: Gravity waves in the mesosphere, Dynamics of the middle atmosphere, pp. 3–18, 1984.

Lindzen, R. S.: Turbulence and stress owing to gravity wave and tidal breakdown, Journal of Geophysical Research: Oceans, 86, 9707–9714, https://doi.org/https://doi.org/10.1029/JC086iC10p09707, 1981.

Maekawa, R.: Observations of gravity waves in the mesopause region by multicolor airglow imaging, Master Thesis, Kyoto University, 2000.

Medeiros, A., Taylor, M. J., Takahashi, H., Batista, P., and Gobbi, D.: An investigation of gravity wave activity in the low-latitude upper mesosphere: Propagation direction and wind filtering, Journal of Geophysical Research: Atmospheres, 108, https://doi.org/https://doi.org/10.1029/2002JD002593, 2003.

Medvedev, A. S., Klaassen, G. P., and Yiğit, E.: On the dynamical importance of gravity wave sources distributed over different heights in the atmosphere, Journal of Geophysical Research: Space Physics, 128, e2022JA031 152, 2023.

Mies, F. H.: Calculated vibrational transition probabilities of OH (X2Π), Journal of Molecular Spectroscopy, 53, 150–188, 1974.

Nappo, C. J.: An introduction to atmospheric gravity waves, Academic press, 2013.

Narayanan, V. L., Wright, C., Mlynczak, M., Hindley, N., Kavanagh, A., Moffat-Griffin, T., and Noble, P.: Observations of mesospheric gravity waves generated by geomagnetic activity, Journal of Geophysical Research: Space Physics, 129, e2023JA032 157, 2024.

Nyassor, P. K., Buriti, R. A., Paulino, I., Medeiros, A. F., Takahashi, H., Wrasse, C. M., and Gobbi, D.: Determination of gravity wave parameters in the airglow combining photometer and imager data, in: Annales Geophysicae, vol. 36, pp. 705–715, Copernicus GmbH, https://doi.org/10.5194/angeo-36-705-2018, 2018.

Nyassor, P. K., Wrasse, C. M., Gobbi, D., Paulino, I., Vadas, S. L., Naccarato, K. P., Takahashi, H., Bageston, J. V., Figueiredo, C. A. O. B., and Barros, D.: Case Studies on Concentric Gravity Waves Source Using Lightning Flash Rate, Brightness Temperature and Backward Ray Tracing at São Martinho da Serra (29.44°S, 53.82°W), Journal of Geophysical Research: Atmospheres, 126, e2020JD034 527, https://doi.org/https://doi.org/10.1029/2020JD034527, 2021.

Nyassor, P. K., Wrasse, C. M., Paulino, I., Gobbi, D., Yiğit, E., Takahashi, H., Batista, P. P., Naccarato, K. P., Buriti, R. A., Paulino, A. R., Barros, D., and Figueiredo, C. A. O. B.: Investigations on Concentric Gravity Wave Sources Over the Brazilian Equatorial Region, Journal of Geophysical Research: Atmospheres, 127, e2021JD035 149, https://doi.org/https://doi.org/10.1029/2021JD035149, 2022a.

Nyassor, P. K., Wrasse, C. M., Paulino, I., São Sabbas, E. F., Bageston, J. V., Naccarato, K. P., Gobbi, D., Figueiredo, C. A., Ayorinde, T. T., Takahashi, H., et al.: Sources of concentric gravity waves generated by a moving mesoscale convective system in southern Brazil, Atmospheric Chemistry and Physics, 22, 15 153–15 177, https://doi.org/10.5194/acp-22-15153-2022, 2022b.

Paulino, I., Figueiredo, C. A. O. B., Rodrigues, F. S., Buriti, R. A., Wrasse, C. M., Paulino, A. R., Barros, D., Takahashi, H., Batista, I. S., Medeiros, A. F., Batista, P. P., Abdu, M. A., de Paula, E. R., Denardini, C. M., Lima, L. M., Cueva, R. Y., and Makela, J. J.: Atmospheric Gravity Waves Observed in the Nightglow Following the 21 August 2017 Total Solar Eclipse, Geophysical Research Letters, 47, e2020GL088 924, https://doi.org/https://doi.org/10.1029/2020GL088924, 2020.

Roach, F. E.: The light of the night sky, vol. 8, Springer Science & Business Media, 2013.

Sato, K. and Yoshiki, M.: Gravity wave generation around the polar vortex in the stratosphere revealed by 3-hourly radiosonde observations at Syowa Station, Journal of the Atmospheric Sciences, 65, 3719–3735, https://doi.org/10.1175/2008JAS2539.1, 2008.

Schöch, A., Baumgarten, G., Fritts, D., Hoffmann, P., Serafimovich, A., Wang, L., Dalin, P., Müllemann, A., and Schmidlin, F.: Gravity waves in the troposphere and stratosphere during the MaCWAVE/MIDAS summer rocket program, Geophysical research letters, 31, https://doi.org/10.1029/2004GL019837, 2004.

Sentman, D., Wescott, E., Picard, R., Winick, J., Stenbaek-Nielsen, H., Dewan, E., Moudry, D., Sao Sabbas, F., Heavner, M., and Morrill, J.: Simultaneous observations of mesospheric gravity waves and sprites generated by a midwestern thunderstorm, Journal of Atmospheric and Solar-Terrestrial Physics, 65, 537–550, https://doi.org/10.1016/S1364-6826(02)00328-0, 2003.

Silverman, S.: Night airglow phenomenology, Space Science Reviews, 11, 341–379, 1970.

Sivjee, G. and Hamwey, R.: Temperature and chemistry of the polar mesopause OH, Journal of Geophysical Research: Space Physics, 92, 4663–4672, 1987.

Snively, J. B. and Pasko, V. P.: Excitation of ducted gravity waves in the lower thermosphere by tropospheric sources, Journal of Geophysical Research: Space Physics, 113, https://doi.org/10.1029/2007JA012693, 2008.

Snively, J. B., Pasko, V. P., Taylor, M. J., and Hocking, W. K.: Doppler ducting of short-period gravity waves by midlatitude tidal wind structure, Journal of Geophysical Research: Space Physics, 112, https://doi.org/10.1029/2006JA011895, 2007.

Suzuki, S., Shiokawa, K., Otsuka, Y., Ogawa, T., Kubota, M., Tsutsumi, M., Nakamura, T., and Fritts, D. C.: Gravity wave momentum flux in the upper mesosphere derived from OH airglow imaging measurements, Earth, planets and space, 59, 421–428, 2007.

Suzuki, S., Lübken, F.-J., Baumgarten, G., Kaifler, N., Eixmann, R., Williams, B. P., and Nakamura, T.: Vertical propagation of a mesoscale gravity wave from the lower to the upper atmosphere, Journal of Atmospheric and Solar-Terrestrial Physics, 97, 29–36, https://doi.org/10.1016/j.jastp.2013.01.012, 2013.

Takahashi, H., Batista, P. P., Buriti, R., Gobbi, D., Nakamura, T., Tsuda, T., and Fukao, S.: Simultaneous measurements of airglow oh emissionand meteor wind by a scanning photometer and the muradar, Journal of atmospheric and solar-terrestrial physics, 60, 1649–1668, 1998.

Taori, A., Taylor, M. J., and Franke, S.: Terdiurnal wave signatures in the upper mesospheric temperature and their association with the wind fields at low latitudes (20 N), Journal of Geophysical Research: Atmospheres, 110, https://doi.org/10.1029/2004JD004564, 2005.

Taylor, M. J. and Hapgood, M.: Identification of a thunderstorm as a source of short period gravity waves in the upper atmospheric nightglow emissions, Planetary and space science, 36, 975–985, https://doi.org/10.1016/0032-0633(88)90035-9, 1988.

Townsend, A.: Internal waves produced by a convective layer, Journal of Fluid Mechanics, 24, 307–319, https://doi.org/10.1017/S0022112066000661, 1966.

Vadas, S. L.: Horizontal and vertical propagation and dissipation of gravity waves in the thermosphere from lower atmospheric and thermospheric sources, Journal of Geophysical Research: Space Physics, 112, https://doi.org/10.1029/2006JA011845, 2007.

Vadas, S. L., Fritts, D. C., and Alexander, M. J.: Mechanism for the generation of secondary waves in wave breaking regions, Journal of the Atmospheric Sciences, 60, 194–214, https://doi.org/10.1175/1520-0469(2003)060<0194:MFTGOS>2.0.CO;2, 2003.

Vadas, S. L., Taylor, M. J., Pautet, P.-D., Stamus, P., Fritts, D. C., Liu, H.-L., São Sabbos, F., Batista, V., Takahashi, H., and Rampinelli, V.: Convection: the likely source of the medium-scale gravity waves observed in the OH airglow layer near Brasilia, Brazil, during the SpreadFEx campaign, in: Annales Geophysicae, vol. 27, p. 231, European Geosciences Union, https://doi.org/10.5194/angeo-27-231-2009, 2009.

Vadas, S. L., Zhao, J., Chu, X., and Becker, E.: The excitation of secondary gravity waves from local body forces: Theory and observation, Journal of Geophysical Research: Atmospheres, 123, 9296–9325, https://doi.org/10.1029/2017JD027970, 2018.

Vargas, F., Swenson, G., Liu, A., and Gobbi, D.: O (1S), OH, and O2 (b) airglow layer perturbations due to AGWs and their implied effects on the atmosphere, Journal of Geophysical Research: Atmospheres, 112, 2007.

Vargas, F., Gobbi, D., Takahashi, H., and Lima, L.: Gravity wave amplitudes and momentum fluxes inferred from OH airglow intensities and meteor radar winds during SpreadFEx, in: Annales Geophysicae, vol. 27, pp. 2361–2369, Copernicus Publications Göttingen, Germany, 2009.

Wrasse, C. M., Takahashi, H., and Gobbi, D.: Comparison of the OH (8-3) and (6-2) band rotational temperature of the mesospheric airglow emissions, Revista Brasileira de Geofísica, 22, 223–231, https://doi.org/10.1590/S0102-261X2004000300002, 2004.

Wrasse, C. M., Takahashi, H., Medeiros, A. F., Lima, L. M., Taylor, M. J., Gobbi, D., and Fechine, J.: Determinaçao dos parâmetros de ondas de gravidade através da análise espectral de imagens de aeroluminescência, Revista Brasileira de Geofísica, 25, 257–265, https://doi.org/10.1590/S0102-261X2007000300003, 2007.

Wrasse, C. M., Nyassor, P. K., da Silva, L. A., Figueiredo, C. A., Bageston, J. V., Naccarato, K. P., Barros, D., Takahashi, H., and Gobbi, D.: Studies on the propagation dynamics and source mechanism of quasi-monochromatic gravity waves observed over São Martinho da Serra (29° S, 53° W), Brazil, Atmospheric Chemistry and Physics, 24, 5405–5431, 2024.

Yamashita, C., Chu, X., Liu, H.-L., Espy, P. J., Nott, G. J., and Huang, W.: Stratospheric gravity wave characteristics and seasonal variations observed by lidar at the South Pole and Rothera, Antarctica, Journal of Geophysical Research: Atmospheres, 114, https://doi.org/10.1029/2008JD011472, 2009.

Yiğit, E. and Medvedev, A. S.: Heating and cooling of the thermosphere by internal gravity waves, Geophysical Research Letters, 36, 2009.

Yiğit, E. and Medvedev, A. S.: Role of gravity waves in vertical coupling during sudden stratospheric warmings, Geoscience Letters, 3, 1–13, https://doi.org/https://doi.org/10.1186/s40562-016-0056-1, 2016.

Yiğit, E., Aylward, A. D., and Medvedev, A. S.: Parameterization of the effects of vertically propagating gravity waves for thermosphere general circulation models: Sensitivity study, Journal of Geophysical Research: Atmospheres, 113, 2008.

Yiğit, E., Knížová, P. K., Georgieva, K., and Ward, W.: A review of vertical coupling in the Atmosphere–Ionosphere system: Effects of waves, sudden stratospheric warmings, space weather, and of solar activity, Journal of Atmospheric and Solar-Terrestrial Physics, 141, 1–12, 2016.

Yiğit, E., Medvedev, A. S., and Ern, M.: Effects of latitude-dependent gravity wave source variations on the middle and upper atmosphere, Frontiers in Astronomy and Space Sciences, 7, 614 018, 2021.

Yue, J., Vadas, S. L., She, C.-Y., Nakamura, T., Reising, S. C., Liu, H.-L., Stamus, P., Krueger, D. A., Lyons, W., and Li, T.: Concentric gravity waves in the mesosphere generated by deep convective plumes in the lower atmosphere near Fort Collins, Colorado, Journal of Geophysical Research: Atmospheres, 114, https://doi.org/10.1029/2008JD011244, 2009.

Yue, J., Miller, S. D., Straka III, W. C., Noh, Y.-J., Chou, M.-Y., Kahn, R., and Flower, V.: La Soufriere volcanic eruptions launched gravity waves into Space, Geophysical Research Letters, 49, e2022GL097 952, https://doi.org/10.1029/2022GL097952, 2022.